

Surface studies of nanomagnetic systems

A thesis submitted to the University of Dublin, Trinity College,
in application for the degree of Master in Science
by

Diarmaid Mac Mathúna

Physics Department
Trinity College Dublin

February 2002

Declaration

This thesis is submitted by the undersigned for the degree of Master in Science at the University of Dublin. It has not been submitted as an exercise for a degree at any other university.

Apart from the advice, assistance and joint effort mentioned in the acknowledgements and in the text, this thesis is entirely my own work.

I agree that the library may lend or copy this thesis freely on request.

Diarmaid Mac Mathúna

February 2002

Acknowledgements

I would like to thank my supervisor, Professor I. V. Shvets, for giving me the opportunity to work on magnetite and other magnetic systems. I would also like to thank the members of the Nanotechnology Group, both past and present, for their assistance and company during the course of my research. In particular, Guido Mariotto introduced me to the physics of magnetite, Dr Shane Murphy showed me how all the equipment worked, Dr Jürgen Osing gave a lot of practical advice, Dr Aidan Quinn explained complicated principles simply and Dr Ciarán Seoighe helped me organise the D.U. Physical Society.

Anselm Gademann, Sergei Makarov, Giuseppe Manai, Victor Oussov, Luca Seravalli, William Signac, and Vivienne Williams have all been helpful over the last couple of years. In addition, Roman Kantor and Dmitry Kashanin have given a lot of technical advice during the course of this project, while Sergio Fernandez Ceballos has produced many of the scanning tunnelling microscopy tips that were used in the experiments themselves.

The staff of the Physics Department have given me considerable support and encouragement during my time in Trinity. Professor W. J. Blau has been a supportive head of department, and I am grateful to the many lecturers and staff in the department who have shared their enthusiasm and knowledge of physics with me. I would like to thank Tom Burke and John Kelly for their assistance during my postgraduate studies. Michelle Duffy, Marie Kinsella, Elaine O'Malley and Susan Priest have always been helpful with administrative matters while James Egan, David Grouse and Michael Reilly

have taught me many important and useful skills in the workshop.

I would also like to thank the many people I met during my work at the Universität Regensburg in Germany for the insights into scientific research that I gained there. They include Prof. Dr. W. Prettl, Dr. V. Novák and Dieter Schowalter.

Many other students, both inside and outside the Physics Department, as well as the members of the D.U. Physical Society have provided a welcome diversion from the world of surface science for which I am grateful. In addition, Michael Conry, Brian Kilbride, Fiachra Ó Brádaigh and Chris Singleton have always been good friends to me. I would also like to thank Aoife Hayden for her friendship and support.

Ba mhaith liom buíochas a ghabháil freisin le mo theaghlach as a dtacaíocht agus as a gcomhairle leanúnach. Buíochas freisin le foireann Raidió na Life 106.4 fm a thaispeáin an saol taobh amuigh den fhisic dom.

Abstract

In this set of experiments, the properties of several nanomagnetic systems have been studied using a variety of surface sensitive techniques. These techniques were used in Ultra High Vacuum (UHV) conditions and include Scanning Tunnelling Microscopy (STM), Auger Electron Spectroscopy (AES) and Low Energy Electron Diffraction (LEED). Several different systems were studied, including thin iron films grown on a molybdenum substrate and both the unpolished and polished faces of an artificial bulk magnetite crystal. Deposition of a 3.6 ML Fe at 800 K on Mo(110) led to the formation of large wedge-shaped islands. Using an antiferromagnetic MnNi STM tip unusual variations in the surface roughness, possibly magnetic in origin, were observed between the islands.

The unpolished (001) plane of an artificial Fe_3O_4 crystal was also studied. Initially, AES revealed the presence of a significant amount of carbon with an atomic concentration of approximately $C_C = 0.94$. Although an anneal temperature of 950 ± 20 K, led to the rapid desorption of the C, it also led to the apparent diffusion of Ca from the bulk to the surface. A faint (1×1) LEED pattern was also observed indicating the presence of the normally unstable polar (001) surface of Fe_3O_4 , possibly due to the stabilizing effect of contaminants. Although the sample roughness made routine STM difficult, large changes in the surface morphology were observed after annealing. Small clusters were consistently observed on the sample surface.

Following the studies of the unpolished magnetite face, the sample was removed from UHV and re-inserted with the polished face exposed. Annealing

sessions at 950 ± 20 K caused C to desorb rapidly from the surface, while the Ca level gradually increased to $C_{Ca} = 0.19$. LEED patterns initially showed the presence of (1×1) termination of the surface. Before additional annealing, unusual long terraces were observed in one area of the sample, possibly due to the slightly different plane of polishing in that region. After a 15 hour anneal, the surface contained dendritic channels 1.9 ± 0.2 Å deep. After annealing the sample for a further 60 hours, linear features or “nanoterraces” appeared with a corresponding $p(1 \times 4)$ reconstruction seen by LEED. The periodicity of these nanoterraces in the $[1\bar{1}0]$ direction was 29 ± 3 Å and 37 ± 4 Å in the $[110]$ direction. The nanoterraces are composed of approximately four atomic rows, spaced 5.4 ± 0.5 Å apart. Further annealing led to a deterioration in STM image quality and a fainter LEED pattern, probably associated with a Ca overlayer. The periodicity of the nanoterraces observed in the $[1\bar{1}0]$ direction was 31 ± 3 Å, and 14 ± 1 Å in the $[110]$ direction.

From these experiments on magnetite, it is apparent that calcium plays a significant role in determining the surface topography. Further investigation of the role of impurities at the surface of magnetite could lead to the development of self-patterned magnetic substrates and templates for nanometre scale magnetic devices.

List of abbreviations

1D - one dimensional

2D - two dimensional

3D - three dimensional

AES - Auger electron spectroscopy

CMA - cylindrical mirror analyser

DOS - density of states

e-beam - electron beam

GMR - giant magnetoresistance

LDOS - local density of states

LEED - low energy electron diffraction

LT - low temperature

LT STM - low temperature scanning tunnelling microscopy

MBE - molecular beam epitaxy

ML - monolayer

RFA - retarding field analyser

RT - room temperature

RT STM - room temperature scanning tunnelling microscopy

SPM - scanning probe microscopy

SP STM - spin polarised scanning tunnelling microscopy

SP STS - spin polarised scanning tunnelling spectroscopy

STM - scanning tunnelling microscopy

STS - scanning tunnelling spectroscopy

TSP - titanium sublimation pump

UHV - ultra high vacuum

XRD - x-ray diffraction

List of Figures

2.1	Schematic diagram of iron morphology	10
2.2	Schematic structure of the magnetite (001) surface	15
3.1	Schematic structure of the piezowalker	25
3.2	Measured pickup on the Tunnel Current Signal	36
4.1	STM Images of the Mo(110) Substrate	39
4.2	STM Images of 1.2 ML Fe Film on Mo(110)	41
4.3	STM Images of 3.6 ML Fe Film on Mo(110)	42
4.4	3D STM Image of Large Fe Island	44
5.1	AES Spectra of Unpolished Magnetite	48
5.2	STM Images of Unpolished Magnetite	53
5.3	3D STM image of Polished Magnetite after a 4 Hour Anneal	55
6.1	AES Spectra of Polished Magnetite	58
6.2	LEED Patterns of Polished Magnetite	62
6.3	STM Images of Polished Magnetite	64
6.4	STM Images of Polished Magnetite after a 15 Hour Anneal	66
6.5	3D STM image of Polished Magnetite after a 15 Hour Anneal	68
6.6	STM Images of Polished Magnetite after a 60 Hour Anneal	70

6.7	3D STM Image of Polished Magnetite after a 60 Hour Anneal	72
6.8	STM Images of Polished Magnetite after a 37 Hour Anneal . .	73

List of Tables

3.1	Piezo Walker Characteristics	28
3.2	Measured Piezo Walker Step Sizes	31
3.3	Measured Tube Scanner Resonance Frequencies	34
5.1	Surface Atomic Concentrations of Unpolished Magnetite	49
6.1	Surface Atomic Concentrations of Polished Magnetite	60

Contents

1	Introduction	1
2	Theory	6
2.1	Scanning Tunnelling Microscopy	6
2.2	Thin Films of Iron	9
2.2.1	Structure and epitaxy	10
2.2.2	Anisotropy	12
2.3	Magnetite	14
3	Experimental Details	18
3.1	Vacuum System	18
3.2	Scanning Tunnelling Microscopes	20
3.3	Data processing	22
3.4	STM Testing Procedures	23
3.4.1	Piezowalker	24
3.4.2	Tube scanner	31
3.4.3	Pre-amplifier	35
4	Iron Films on Molybdenum	38
4.1	Mo(110) Substrate	39

4.2	1.2 ML Fe on Mo(110) at 315 K	40
4.3	3.6 ML Fe on Mo(110) at 800 K	42
5	Unpolished Magnetite Surface	46
5.1	AES analysis	47
5.2	LEED patterns	51
5.3	STM images	52
6	Polished Magnetite Surface	57
6.1	AES analysis	58
6.2	LEED patterns	60
6.3	STM images	63
6.3.1	15 Hour Anneal	65
6.3.2	60 Hour Anneal	69
6.3.3	37 Hour Anneal	71
6.4	Overview	74
7	Conclusions	76
7.0.1	Unpolished Magnetite Surface	77
7.0.2	Polished Magnetite Surface	79
7.1	Further Work	84

Chapter 1

Introduction

Magnetism plays a central role in many aspects of everyday life. Many living organisms, including humans and magnetotactic bacteria, have used magnetic materials such as magnetite for navigation [1]. Magnetite is also believed to have played a central role in catalysing important synthesis steps that led to the formation of the first complex biological molecules, and continues to be used in the production of ammonia in industry [2].

In recent decades, magnetic recording devices have been developed that store information in magnetic materials. As the pressure to store more and more information in smaller spaces has grown over recent years due to advances in computing power, research has concentrated on the properties of small magnetic structures and systems. An understanding of the properties of these systems as they are miniaturised is vitally important both for the industrial companies producing them and for the insight they offer the scientific community into the fundamental physics of magnetism.

Magnetic systems continue to be studied intensively because of the new insights being gained into their fundamental physical properties on the nanome-

tre scale as well as their technological importance in fields such as magnetic recording and spin electronics [3]. The surfaces of such magnetic systems are particularly important in determining their behaviour and interaction with their surroundings. In addition, advances in the production of thin films have led to their features being studied in structures exhibiting magnetic, superconducting [4] and other properties.

This study has used a wide variety of sensitive experimental techniques to probe the surface properties of several magnetic systems on the scale of nanometres. Thin films of iron grown on a substrate of the metal molybdenum have been studied. Both the polished and unpolished faces of an artificially grown crystal of the mineral magnetite have also been investigated.

There are several mentions of magnetite (also known as loadstone or lodestone) in ancient Irish texts, and the earliest reference dates from around 1000 AD [5]. In a poem on the geography of the world, the poet Airbertach Mac Coisse describes the “goods” of India and includes “magnéit” or magnetite as well as “adamant” among them. It is interesting to note that the earliest reference to magnetite in English is over four hundred years later, in 1440 AD, when a reference is made to “Magnetete, precyowse stone” [6]. This discrepancy may be due to the confusion caused by references to the apparently non-existent mineral known as “adamant” which was reputed to have the properties of both magnetite and diamond.

Magnetic nanostructures have become centres of great interest in the scientific community and in industry as the core technologies behind magnetic recording devices. The investigation of the properties of magnetic systems on the nanometre scale has led to a better understanding of the fundamental

physics of magnetism and the improvement of technological materials used in magnetic recording devices. Indeed, the development of hard disk recording heads based on the phenomenon of giant magnetoresistance (GMR) in magnetic nanostructures [7] has been one of the physics success stories of recent decades, and involved the study of 30,000 different multilayer combinations of elements [8].

A wide variety of techniques have been developed to study the properties of surfaces. Among the techniques used to study the contaminants that adsorb onto the surface are atomic force microscopy (AFM), Raman spectroscopy (RS) [9], core level photoemission spectroscopy [10], soft X-ray photoelectron spectroscopy (SXPS) [11] and resonant optical second harmonic generation (SHG) [12]. Sophisticated techniques have also been developed to analyse the magnetic properties of small magnetic structures and surfaces. They include transmission electron microscopy (TEM) [13], the Mössbauer effect [14], and X-ray magnetic circular dichroism (XMCD) [15]. In addition, scanning probe techniques based on optical [16–18] and other effects [19], and in particular scanning tunnelling microscopy (STM) [20] have provided high resolution images of surfaces in recent decades.

The use of magnetically sensitive STM tips also leads to the possibility of imaging magnetic structure on the nanometre scale [21]. Several different techniques have been devised in order to investigate the magnetic properties of such systems with scanning probe techniques, and among them are Spin Polarized Scanning Tunnelling Microscopy (SP-STM) and Spin Polarized Scanning Tunneling Spectroscopy (SP-STs) [22].

Although magnetite has been studied extensively [23], the complexity

of its surface structure has only been appreciated since ultra high vacuum (UHV) systems have enabled detailed studies of the surface to be carried out. The experimental techniques used in this project to investigate the surfaces of magnetic systems include Auger electron spectroscopy (AES), low energy electron diffraction (LEED) and scanning tunnelling microscopy (STM). The central technique used in this project is STM as it provides a high-resolution topographic image of the sample surface. During the course of this project, a comprehensive set of procedures has been developed that enable the characteristics of an STM to be determined quantitatively as well as the systematic troubleshooting of the experimental setup. The properties that can be measured include the size of steps taken by the piezowalker coarse positioner in the STM head and the resonance frequencies of the tube scanner.

This work has built on the previous work done in the Physics Dept of Trinity College, Dublin as well as more recent research [24–26]. The continued development of the equipment used to study the magnetic systems in the Nanotechnology Group in Trinity College, Dublin has meant that analysis by new techniques can usefully contribute to a more complete understanding of the results from previous experiments. Research in other groups has also focussed on the properties of thin films of iron oxides, and these are closely related to the characteristic surface structures found in the bulk samples of magnetite studied here [27].

The samples studied include thin films of iron on molybdenum as well as magnetite in its single crystal form. Iron films of different thicknesses have been grown on a vicinal Mo(110) substrate at two different temperatures in order to study the influence of temperature and deposition rate on their

growth modes, and an antiferromagnetic MnNi tip has been used to investigate the feasibility of spin polarised STM (SP STM).

Both the polished and unpolished faces of an artificially grown Fe_3O_4 single crystal oriented in the (001) plane were studied. A number of surface structures including linear features referred to as “nanoterraces” were observed by STM, and it is probable that they are associated with the presence of contaminants such as carbon and calcium. It appears that C adsorbs onto the surface during the sample preparation, while heating of the sample during lengthy annealing stages leads to the diffusion of Ca from the bulk of the crystal to the surface.

The experimental results described here provide new insights into the morphology of nanomagnetic systems as well as the factors that influence their topography. It is hoped that this research will give new insights into the electronic and magnetic properties of magnetite single crystals and iron oxide thin films and lead to a greater understanding of the properties of magnetic systems on the nanometre scale.

Chapter 2

Theory

Many branches of surface science are included either directly or indirectly in this project. They include scanning tunnelling microscopy, the growth of thin films, the properties and structure of magnetite as well as the magnetic characteristics of nanomagnetic systems. In this chapter, a concise introduction to the theoretical background of these topics will be given as well as a comprehensive set of references containing more in-depth analyses.

2.1 Scanning Tunnelling Microscopy

In scanning tunnelling microscopy (STM), a sharp tip is brought very close to a conducting sample. Electrons can travel across this gap by quantum mechanical tunnelling, because their waveform decays exponentially from the sample surface. The tunnelling current depends on the bias voltage applied to the tip and on the probability of finding a tip electron at the surface. This probability is the square of the amplitude of the wavefunction and the tunnelling current can then be written as a function of the sample surface

local density of states (LDOS) at the Fermi level. This leads to the following equation:

$$I \propto V \rho(0, E_F) e^{-2\kappa W} \quad (2.1)$$

where I is the tunnelling current, V is the applied bias between tip and sample, $\rho(0, E_F)$ is the LDOS at the sample surface at the Fermi level E_F , κ is a value proportional to the square root of the work function of the sample surface, and W is the distance between the sample and tip [28]. With a typical value of the work function of 4 eV, this equation leads to a decay in the tunnel current by about an order of magnitude for every Å that the gap is increased. It is this sensitivity to the gap distance that enables the STM to accurately map the topography of the sample surface with atomic resolution. This can be achieved either in constant current mode by moving the tip up and down while it scans the sample maintaining a fixed current, or in constant height mode where the tip is held at a fixed height and the variations in tunnel current measured.

The approximation above neglects however the influence of the tip local density of states on the tunnelling current. Analysis of the tip-sample system by the Bardeen approach shows that the electronic structure of both the tip and the sample are equally important in determining the tunnelling current. Their symmetrical contribution is shown in the following equation, where ϵ represents a small amount of energy and is the independent variable of integration:

$$I \propto \int_0^{eV} \rho_S(E_F - eV + \epsilon) \rho_T(E_F + \epsilon) d\epsilon \quad (2.2)$$

Using a metal tip, the density of states (DOS) of the tip can be kept constant. This enables the DOS of the sample to be determined by measuring I as a function of V , and then calculating dI/dV :

$$\frac{dI}{dV} \propto \rho_S(E_F - eV) \quad (2.3)$$

It is this relation that forms the basis of scanning tunnelling spectroscopy or STS. This technique can be performed during a normal constant current topographic scan, for example by temporarily disabling the feedback loop controlling the tip-sample separation. The tip is then held at a constant height above a certain point on the sample while the bias voltage is varied and the tunnel current measured. This data can then be compared with the topographic image giving an insight into the surface states of different locations on the sample. However, as the electronic structure of individual STM tips is generally not known, the interpretation of STS results can be difficult. Techniques are continually being developed that enable the reproducible production of well characterised tips, and novel tip structures such as those involving carbon nanotubes at their apex are being investigated [29–31].

Spin polarised STM and STS rely on the spin polarised electronic structure of magnetic systems [7, 32, 33]. Half-metals are conducting materials, but only one polarisation of electrons contributes to this conductivity. The electrons with the opposite spin orientation have less occupied states at the Fermi level. By choosing the correct bias voltage, the spin states of a certain polarisation can in principle be selectively probed [22]. Tips with magnetic properties can also be used to ensure that the tunnelling current depends on the orientation of spins in the sample, as an external magnetic field can be

applied to determine whether the observed effects are indeed magnetic [25]. This external magnetic field causes a change in the spin configuration at the sample surface and enables the separation of spin polarized effects from other contributions to the tunnel current signal. Ferromagnetic tips such as those made from Fe have a large stray field which can influence the magnetisation of the sample and are also prone to magnetostriction which can lead to instrumental artifacts. Antiferromagnetic tips on the other hand do not have this stray field, and should exhibit a significant spin-ordering at the apex of the tip, enabling spin polarised STM (SP STM) to be achieved [21, 34].

2.2 Thin Films of Iron

Thin iron films have magnetic properties which depend on the morphology of the film. These properties make them useful samples with which to investigate various aspects of spin polarised STM. This section will give an overview of the magnetic properties of very thin films (also known as ultra thin films), which are between one and ten monolayers thick.

The iron on molybdenum (110) system, referred to as Fe/Mo(110), has not been studied as intensively as the similar iron on tungsten (110), or Fe/W(110), system [35]. By growing these films on a substrate of vicinal molybdenum (110), iron islands of various sizes and thicknesses can be formed. In particular, the stepped nature of the Mo (110) substrate allows wedge shaped iron islands whose thickness varies along the length of the island to be grown. These wedge shaped islands arise naturally and their structure is shown schematically in Figure 2.1a. Such islands are predicted to have regions with different magnetisation directions.

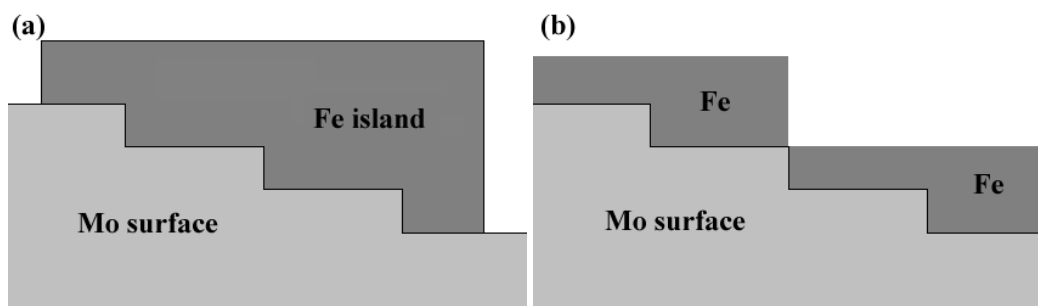


Figure 2.1: These are schematic diagrams of some of the structures formed by iron films on the stepped molybdenum surface. (a) A cross section of naturally occurring wedge shaped islands grown on stepped surfaces in this study. (b) A cross section of an iron film showing how alternate terraces have different thicknesses.

Thin films have been a topic of much interest over the last number of decades. With the movement towards greater data storage densities in computer disk drives, attention is being focussed on the magnetic properties of these films. The way in which film properties differ from those of bulk samples will be discussed here. As the structure of ultrathin films has a strong influence on their magnetic properties, the manner in which ultrathin films grow is discussed initially, and the theory behind their unusual magnetic anisotropies is then described.

2.2.1 Structure and epitaxy

The magnetic properties of thin films are strongly influenced by their structure. Therefore it is useful to describe the manner in which they grow before discussing their magnetic properties. The thin films discussed here are grown epitaxially, that is each crystal in the film grows in a unique orientation

on a single-crystalline substrate. If both materials are the same then this is referred to as auto- or homo-epitaxial growth, and if they are different it is referred to as heteroepitaxial. Thin films rarely grow in a layer-by-layer manner because of the strains caused by depositing the film and substrate materials on top of one another.

The growth modes of crystals can be classified into the following modes [36].

1. **Frank-van der Merwe (FM) growth**

Layer-by-layer growth where complete monolayers are formed before subsequent layers nucleate – the growth is two dimensional (2D).

2. **Volmer-Weber (VW) growth**

Small clusters nucleate on the substrate forming islands in a three dimensional (3D) manner.

3. **Stranski-Krastanov (SK) growth**

A growth mode combining both the VW and FM modes. Initial growth is layer by layer but after a critical thickness is reached, islands form on top of the layers. This is sometimes referred to as 2D \rightarrow 3D growth.

The growth modes can be considered as a wetting problem, governed by the following equation based on the surface energies of the film (σ_A), substrate (σ_B), interface (σ^*) and lattice mismatch (σ_S).

$$\Delta\sigma = \sigma_A - \sigma_B + \sigma^* + \sigma_S \quad (2.4)$$

The growth begins as a monolayer if $\Delta\sigma < 0$ and as islands if $\Delta\sigma > 0$. Plane FM growth is very rare because of the strain energy or lattice mismatch

term that must be included in the surface energies of Equation 2.4. However if the growth is induced by supersaturation (i.e. either low substrate temperature or high evaporation rates) then monolayer nucleation can occur and a forced layer or quasi-FM growth mode results. Kinetic principles govern the growth in most real growth processes and condensation at low temperatures results in small grain sizes while that at high temperatures results in large grains.

The lattice misfit, f , which plays an important role in determining the structure of films, can be defined in a one dimensional (or 1D) model as:

$$f = \frac{(b - a)}{a} \quad (2.5)$$

Where a and b are the lattice parameters of the substrate and film respectively. This misfit results in dislocations and elastic strain, which have important consequences for the magnetoelastic anisotropy of ultrathin films.

2.2.2 Anisotropy

The unusual anisotropies of thin films are an important property both for applications as magnetic recording media and as sources of long range magnetic order. Anisotropy is defined as the contribution to sample free energy that depends on the direction of the magnetization vector \mathbf{M} . Anisotropy results from the crystalline electrostatic field (reflecting the local symmetry of the crystal) influencing the orbits of the electrons in the atoms, which in turn interact with the magnetization through spin-orbit coupling. Uniaxial anisotropy is the simplest example of anisotropy, and in this case it is favourable for \mathbf{M} to lie along an easy axis denoted by z . This axis is the c-axis

in hexagonal, tetragonal and rhombohedral crystals. In acicular (i.e. needle shaped) particles z is along the long axis. Ultrathin film structures exhibit strong uniaxial anisotropies linked with the uniaxial crystal-field interaction at their surfaces and interfaces.

The perpendicular magnetization often found in systems such as Fe/Ag(001), Ni/Cu(001) and Co/Pd can be understood qualitatively by considering the difference in the electronic structure when compared to the bulk, as discussed by O’Handley [37]. In the bulk, the electrons can have components of momentum in any direction (although some directions are favourable based on the shapes of the orbitals). As it is unlikely to find d electrons outside the surface of the film, the components of electron momentum perpendicular to the surface are reduced. The velocity in the surface plane is linked to the angular momentum perpendicular to the surface and this causes the quantity $\frac{L_z^2}{L_x^2+L_y^2}$ to increase near the surface. In situations where the spin-orbit coupling is significant the component of the spin perpendicular to the surface will increase — and therefore perpendicular magnetization is favoured.

The various anisotropy contributions can be categorised as [36,38]:

- shape anisotropy
- bulk magnetocrystalline anisotropy
- strain anisotropy
- magnetic surface anisotropy

2.3 Magnetite

Although the chemical formula for magnetite, Fe_3O_4 , is relatively simple, its actual structure is quite complex as can be seen in the schematic diagram shown in Figure 2.2. Magnetite forms crystals in the cubic inverse spinel structure. In this structure, the oxygen O^{2-} anions form a face centered cubic (fcc) framework and the iron cations (which are present in both their Fe^{2+} and Fe^{3+} form in magnetite) are located in the interstices or gaps of the oxygen frame. All the Fe^{2+} ions and half of the Fe^{3+} ions are in octahedral interstices. The other half of the Fe^{3+} ions are in tetrahedral interstices. The formula unit of magnetite, Fe_3O_4 , can be written more fully as $Fe^{3+} \downarrow [Fe^{3+} \uparrow Fe^{2+} \uparrow] O_4$ where the iron ions enclosed by square brackets are in octahedral interstices.

The cubic unit cell of magnetite contains 8 formula units, that is 32 O^{2-} anions as well as 16 Fe^{3+} and 8 Fe^{2+} cations. The length of the cube side is 8.4 Å. The (001) plane can be viewed as a stack of two alternating layers. One of the layers contains tetrahedral irons, while the other layer is composed of rows of iron ions surrounded by oxygen ions and is shown schematically in Figure 2.2. The rows run perpendicular to one another in neighbouring octahedral layers.

The oxygen lattice is flexible and readily accommodates cations other than iron, and therefore magnetite is often non-stoichiometric [23]. A wide range of cations can be introduced into magnetite. Some elements such as Co, Ni and Zn appear to randomly replace octahedral Fe^{2+} throughout magnetite crystals. Other elements, however, such as Cu, Mn and Cd appear to be concentrated near the surface of the crystals. Fully substituted ferrites have

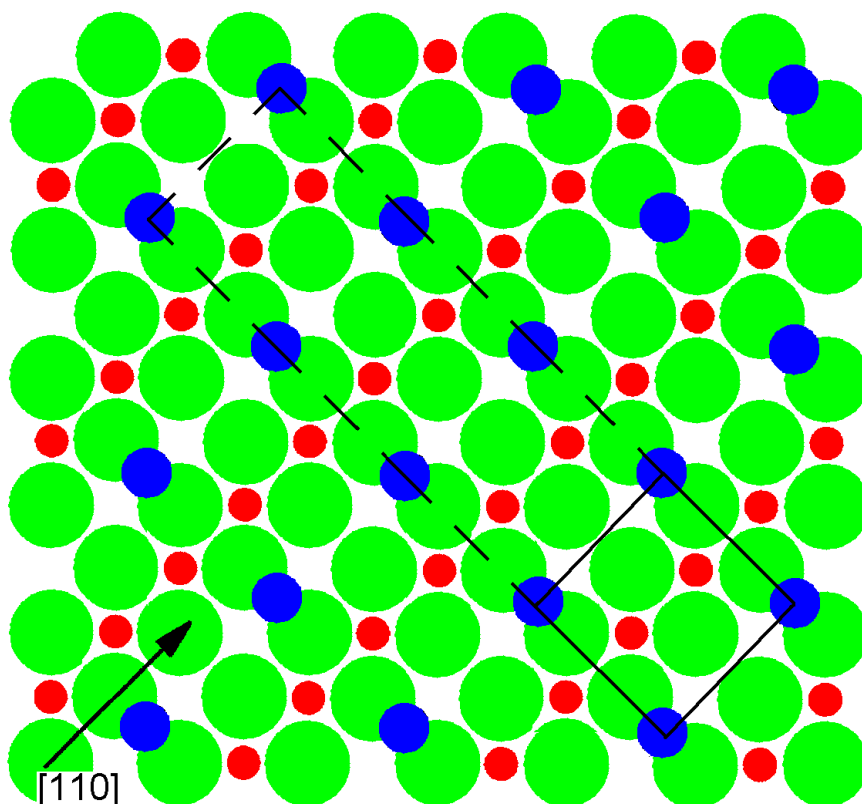


Figure 2.2: This is a schematic of the bulk-terminated Fe_3O_4 (001) surface. The oxygen ions are coloured green, while the octahedral iron ions in the same layer as them are coloured red. The other iron ions which are in the tetrahedral positions on adjacent layers are coloured blue. After Reference [27].

also been produced with a general formula of MFe_2O_4 . Calcium substitution has been found to lead to the cubic cell edge increasing from 8.39 Å to 8.47 Å. Aluminium on the other hand leads to a reduction in the cell edge length, and the influence of aluminium substitution on its magnetic properties has also been studied [23]. Na has also been incorporated into the magnetite structure.

The lattice of iron ions in the tetrahedral positions have their spins aligned parallel with one another but are anti-parallel to the iron ions in the octahedral positions. These two interlocking lattices have unequal magnetic moment and the antiferromagnetic coupling between them does not entirely cancel out the magnetisation of the crystal. This form of magnetism is termed ferrimagnetism. The antiferromagnetic coupling via the $127^\circ Fe_A - O - Fe_B$ bond is stronger than coupling on the octahedral sites. The easy magnetization direction of magnetite also lies along the eight [111] cube diagonals [39], and it has a Curie temperature of 850 K [23].

Magnetite can have metal vacancies on the octahedral sites and it is a semi-conductor with a band gap of about 0.1 eV. This band gap is low enough for the thermal energy of the electrons at room temperature to create some conductivity. The high conductivity of magnetite at room temperature is unusual for iron oxides and is due to the hopping of electrons of equal spin between the Fe^{2+} and Fe^{3+} cations in the octahedral sites. At low temperatures, however, electron delocalization is inhibited and this hopping is frozen out and the conductivity decreases by approximately two orders of magnitude in stoichiometric crystals [26]. The temperature at which this transition occurs is called the Verwey temperature (T_V) and is typically around 118 K

for stoichiometric single crystals of magnetite [23]. The Verwey temperature varies with the stoichiometry of the sample and is often used as a method to check for the presence of impurities which can lead to the point of the transition falling to about 100 K [26, 40, 41]. Magnetite has been studied by low temperature STM close to the Verwey temperature at 125 K [42].

The focus of the current project has been on the (001) plane of magnetite. Previous studies have focussed on mechanically polished magnetite crystals only, and it has been shown previously that the optical properties of spinels such as magnetite are effected by the form of polishing used [25, 43]. In this study, both the polished and unpolished sides of an artificially grown bulk magnetite crystal have been studied. The (001) plane has square four-fold symmetry and the topography of crystals cut along this plane consists of many square terraces. It has been found that the surface of magnetite is very sensitive to the preparation conditions and that it reconstructs into several different forms depending on the way in which it was prepared. Some linear reconstructions observed by STM on magnetite have been attributed to the presence of contaminants such as Mg, Ca or K [26, 27], although it was thought previously that similar surfaces were stoichiometric [24, 25].

A Wigner glass state is reported to occur on the Fe_3O_4 surface at room temperature, and the resulting charge ordering at the surface has been studied on the atomic scale using SP STM [26, 44]. This surface continues to be an interesting candidate for the further investigation of spin polarized phenomena.

Chapter 3

Experimental Details

Several different experimental methods were used during this project. In this chapter, an overview of these experimental techniques and their associated data processing systems will be given. A comprehensive set of procedures developed during this project will also be outlined that enable the testing and quantitative analysis of scanning tunnelling microscopes, and other similar scanning probe technologies. Note that in order to emphasise that the individual chambers in the vacuum system used in this study are distinct units, their names have been capitalised when they are referred to in the text.

3.1 Vacuum System

The experiments performed in this study were carried out in an ultra-high vacuum (UHV) system. This system consists of three separate chambers, separated by valves and has been described in detail elsewhere [25, 45]. The system is pumped by a combination of roughing and turbo-pumps, non-evaporable getter (NEG) pumps, liquid nitrogen cooled titanium sublimation

pumps (TSPs) and by several ion-pumps. The base pressure in the system is typically in the low 10^{-10} mbar range. A fast-entry load lock chamber is connected to the Preparation Chamber where most sample preparation is carried out. The Preparation Chamber is equipped with a number of devices for the cleaning of samples and deposition of thin films. These include an electron beam or e-beam heater (for quickly heating or flash-annealing refractory metals such as molybdenum), a resistive heater (for heating samples such as magnetite for long periods of time), and an argon ion gun that is used to clean both the samples themselves and the STM tips [46]. An e-beam evaporator that was developed in-house was used to deposit the thin iron films described in this study. This unit has recently been upgraded to a commercial Omicron EFM-3 device. The preparation chamber also contained an Auger Electron Spectroscopy (AES) instrument for determining the chemical composition of the sample surface to be investigated [47]. This AES equipment is more sensitive than the instrument that was available to previous researchers in the Nanotechnology Group [25].

The evaporation of iron was monitored by a quartz crystal monitor supplied by Inficon. This device measures the mass of the iron incident on the quartz crystal, and then calculates a thickness deposition rate in units of $\text{\AA}\cdot\text{s}^{-1}$ based on the assumption that the Fe is growing in the bcc structure. From the thickness value determined by the Inficon monitor, the fractional coverage of the iron in units of pseudomorphic monolayer equivalent (ML) can be determined, as well as the deposition rate in units of $\text{ML}\cdot\text{min}^{-1}$, as described in detail in Reference [48].

An external pyrometer is used to monitor the temperature of the sample

being flash-annealed in the e-beam heater. It is an Ultimex UX-20, with a temperature range of approximately 900 – 3300 K. The emissivity value (ϵ) of molybdenum used is taken from the manufacturer’s manual, and for this model of pyrometer $\epsilon = 0.35$ for the “mirror quality” finish of the sample studied here.

3.2 Scanning Tunnelling Microscopes

A Low Temperature STM Chamber and a Room Temperature STM Chamber are connected to the Preparation Chamber. The Low Temperature STM (LT STM) consists of an STM head made from the machinable ceramic Macor which can be lowered into a cryostat, as described in Reference [42]. Extensive calibration and performance assessment of this STM was carried out during the course of this project. The Room Temperature STM Chamber contains the Room Temperature STM (RT STM) made from Macor. It was this RT STM that was used for most of the scanning sessions in this set of experiments, and it was also calibrated and tested extensively as part of this project. The Room Temperature STM Chamber is also equipped with a Low Energy Electron Diffraction (LEED) system which can be used to determine the crystal structure of a sample surface.

The STMs are controlled by computerized external control units, which control the position of the tip relative to the sample and acquire data during the scanning sessions. The control system used initially was a WA Technologies Tops II unit. This Tops unit was upgraded to a newly commissioned Omicron Scala Control Unit during the course of this project. The Scala controller was calibrated in the $x - y$ plane by obtaining atomic resolution on

flat highly oriented pyrolytic graphite (HOPG). Vertical calibration was done using the monatomic steps on a vicinal Mo(110) sample. The calibration was also determined by comparison with the values determined for the original Tops controller. Several problems were encountered while commissioning the Scala unit, and it is possible that the system has not yet been fully optimised. After intensive discussions with Omicron representatives, it appears that any discrepancy in the lateral calibration of the Scala unit compared to the Tops unit could be due to the intrinsic electronic (as opposed to piezo) drift in the control unit. This topic is discussed in Reference [26]. The magnitude of this drift during small area scans can be reduced by changing the range of the scanning speeds available. It is also possible that the value measured by the Scala analog to digital converters for the tunnel current may be different from the actual tunnel current by a factor of two as the pre-amplifier used in the STMs is different from the configuration supplied by Omicron. This feature of the Omicron unit does not however affect the feedback loop controlling the position of the STM tip. In addition, as the optimal tunnel current generally varies both with the sample and the tip it does not affect the images scanned significantly.

It is interesting to note that although atomic resolution can be normally achieved on HOPG, the interpretation of these images is not straightforward. Many different surface topographies have been imaged on graphite [49–51].

The STM tips used in this project were mainly made from tungsten (W), although tips made from the antiferromagnetic material manganese nickel (MnNi) were also used. Mechanically cut PtIr tips were also used. These tips were prepared in-house by the author, Sergio Fernandez Cebal-

los, Guido Mariotto and Dr Shane Murphy. The chemical-etching techniques used are similar to those described in detail elsewhere [48, 52, 53]. After the tips were introduced into the UHV system they were bombarded with argon ions using an ion gun to remove any oxidised layer of material and to improve their shape. The antiferromagnetic MnNi tips enable the feasibility of Spin-Polarized STM to be studied. Other groups have produced tips with similar antiferromagnetic characteristics by depositing thin films of Cr onto conventional W tips [34]. Ferromagnetic tips made from Ni have also been produced [54]. Many different techniques exist to produce reliable tips for STM [55].

3.3 Data processing

A wide variety of powerful processing algorithms are now available to process experimentally acquired data, including STM images, AES spectra and LEED patterns.

In order to provide a range of techniques with which to process STM images, it was decided to use the freeware WSxM image processing software supplied by Nanotec Electronica on their website (<http://www.nanotec.es>) in conjunction with the SPM Software supplied by Omicron. Frequent communication was made with the developers of the WSxM program in order to adapt it to the various STM image data formats used in this project. These discussions have also led to significant improvements to some of the program's features. Both these programs allow the images to be processed and analysed using standard techniques. These techniques include various types of plane fitting of the image which enable the slope of the sample to

be subtracted from the image, as well as analytical tools used to determine quantitative values from the images. For example, local plane fits subtract a slope from the image based on the slope of particular terraces, and this can be used to emphasise the height differences between terraces or steps on the sample. In addition, two dimensional fast Fourier transforms (2D-FFT) can be used to filter unwanted signals with well defined frequencies such as electrical noise or resonance from an image, and line profiles can be used to measure the periodicity and corrugation of features on the surface.

STM images are not the only forms of experimental data which benefit from computerisation. LEED patterns continue to be photographed with a conventional camera but the developed negatives are now scanned directly into a computer where they can be processed to improve the contrast before being printed, a procedure which has led to significant time savings. The data files containing Auger spectra can now be processed using software which was developed as part of this project. This software identifies and labels the most prominent peaks in the spectrum facilitating their identification by comparison with published reference spectra.

3.4 STM Testing Procedures

The testing and performance assessment of scanning tunnelling microscopes has traditionally been qualitative rather than quantitative. Previously published STM evaluation methods are complicated, and difficult to apply in practical situations [56–58]. In order to provide a more rigorous basis for the comparison of different STM setups, a comprehensive set of performance assessment procedures has been developed as part of this project. These pro-

cedures provide a sound theoretical and experimental basis for determining critical factors such as the resonance frequencies of the piezoelectric tube scanner and the step size of the coarse approach piezowalker. In addition, these procedures can also be used to diagnose and troubleshoot many common problems encountered during the use of a scanning tunnelling microscope. These tests provide a firm foundation for the development of new microscopes and the full optimisation of those currently available, including both the Low and Room Temperature STMs. These procedures can also be adapted for the analysis of other instruments based on scanning probes and piezo tube scanners.

3.4.1 Piezowalker

A piezowalker is usually employed in scanning tunnelling microscopes to position the sample close to the STM tip. The sample is initially placed in a holder on the walker several centimetres from the tip, and then raised until that distance has been reduced to approximately 1 mm. An automated procedure called the “auto-approach” is then followed by the control unit to gradually bring the sample within range of the tube scanner without crashing the tip into the sample.

The piezowalker employed in the STMs used in this project consist of six piezo stacks pressed by a spring against a sapphire rod that supports the sample as shown in Figure 3.1, and described by Quinn [45]. A high voltage sawtooth-like waveform is applied to the piezos, and their shearing motion results in a “slip-stick” action which moves the sapphire rod [59, 60]. The thickness and number of piezos “tiles” in each stack of the walker varies in

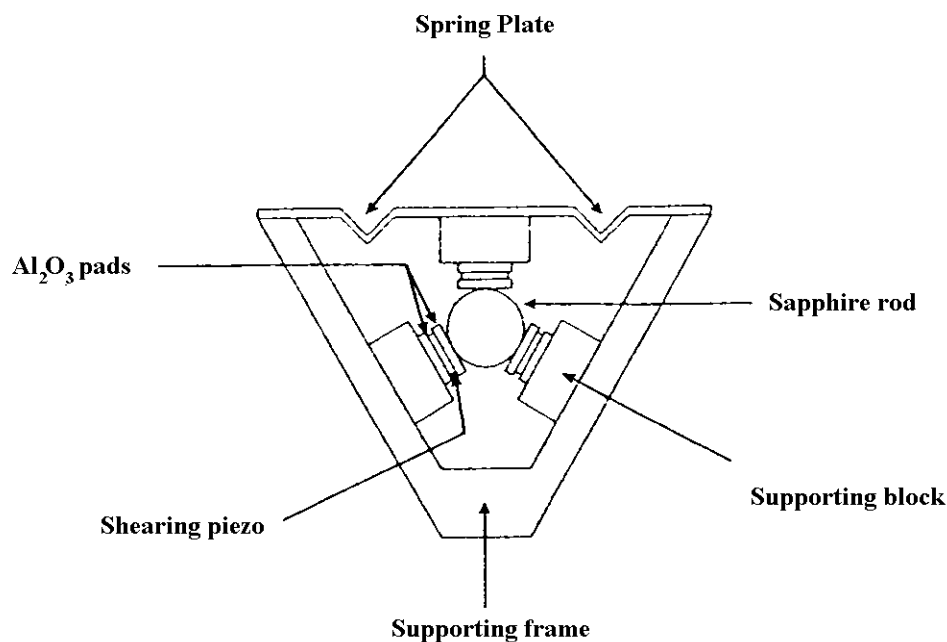


Figure 3.1: This diagram shows the schematic structure of the piezowalker used in the STMs in this project. After Mariotto et al [60].

each STM and several factors contribute to the choice of stack structure. For example, at low temperatures the piezoelectric shearing coefficient is orders of magnitude less than that at room temperature, and more piezos are needed in each stack to achieve a practical step size. In addition, it has been found that the shearing voltage must change very quickly for the piezos to shear at low temperatures [42]. This rate of change, also referred to as the slew rate, must be of the order of microseconds for the piezowalker to function under cryogenic conditions.

Rotational movement can also be incorporated into the piezowalker by varying the orientation of the piezoceramic slices that form each stack. For example, this has been implemented in the Titanium Room Temperature

STM (Ti RT STM) [25]. Another factor determining the stack structure is the thickness of the piezoelectric ceramics used. The highest voltage that can be applied to a piezo tile is proportional to its thickness and this must be taken into account when choosing the stack structure.

Given the variety of piezowalker designs implemented and the various operating temperatures at which they are used it is useful to develop a set of tests that would enable the comparison of the different walker configurations and to facilitate the troubleshooting of problems associated with them. It should be borne in mind that very high voltages (up to 800 V peak to peak) are applied to the piezowalker during its operation and therefore the control unit should be disconnected fully from the STM head before it is manipulated either with bare hands or vacuum wobblesticks.

Basic tests

During normal operation, the coarse positioning circuitry of the Omicron Scala controller applies a high voltage sawtooth-like waveform simultaneously to each of the piezo stacks used for vertical movement. This mode of operation differs from the sequential shearing mode used by the walker electronics connected to the Tops unit. These two modes of operation result in different step sizes and have been compared in detail in other studies [60].

The frequency of the high voltage signal can be set on the Scala to be between 500 Hz and 4 kHz. In order to test the functionality of the walker two basic tests can be applied. First of all, a simple visual check can be made to see whether the walker moves at a satisfactory speed when a high voltage signal is applied to it. At a frequency of 4 kHz this movement should be

several millimetres per second. In addition, the high frequency vibrations of the piezo stacks should be audible if the STM head is in air. In UHV, these vibrations will also be audible if the STM head is mechanically clamped in place as the clamp will transmit the vibrations to the air side of the chamber.

Several factors can prevent the piezowalker from moving even when a voltage is being applied. Each piezowalker has a characteristic threshold voltage below which the sapphire rod will not move. There is also a maximum voltage which can be applied to the piezos - exceeding it will result in the depoling of the piezos and a loss of functionality. This voltage is referred to as the depoling voltage, and for the shearing mode piezos used in the piezowalker described here, this is typically half the value of the depoling voltage for a thickness mode piezo. The piezos used in the STMs described here are EBL#2, and were provided by Stavely Sensors.

These characteristics of the piezowalkers are given in Table 3.1. Typically one side of each piezo tile is grounded and the threshold voltage quoted is a peak-to-peak voltage. For example, for a piezo tile 0.5 mm thick, a voltage of 50 V indicates that one electrode on each piezo is kept at 0 V while the other varies between -80 V and +80 V. This piezo tile will only be depoled if the voltage applied is less than -150 V or greater than +150 V.

As the piezostacks share a common ground, if this ground becomes disconnected the applied voltage will have no effect. Typically, the signal needs to reach at least three of the piezostacks for the sapphire rod to be moved. Depending on its position in the piezowalker, the sapphire rod moves at different velocities, and this is probably due to variations in the surface roughness of the sapphire rod. In the case of the non-cylindrical rods used in some of the

Table 3.1: Piezo Walker Characteristics

<i>STM Name</i>	<i>Piezo Thickness (mm)</i>	<i>Piezos in each Stack</i>	<i>Depoling V Amplitude(V)</i>	<i>Threshold V_{pp} (V)</i>
RT STM	1	1	300	250
LT STM	0.5	4	150	160
Ti RT STM	0.5	2 vertical + 1 rotational	150	160

STMs, the flat part of the rod against which the spring presses may become rotated away from the spring and the force applied by the spring itself to the sapphire rod may also be insufficient or too great. The adjustment of the sapphire rod position and the spring force may lead to movement of the rod, in this case.

Step size measurement

The size of steps taken by the piezowalker is one of its most important characteristics as it determines the duration of an auto-approach procedure, when the tip is initially brought close to the sample. This is particularly significant at low temperatures when the shearing motion of the piezos is quite small. Ideally, the step size while the walker is moving the rod up should be the same as when it is moving the rod down. In the configuration used in the STMs involved in this project, the walker is used to move the sample vertically (unlike some commercial systems which have the sample mounted

horizontally). Gravity plays an important role in this configuration and in practice the ratio of step sizes in the up and down directions is less than one. It is useful to quantify this ratio, and to relate it to a physical step size in order to characterise a specific piezo walker. For this purpose, the procedures outlined below have been developed.

If the STM head is in air, or the distance between certain points on the STM head body are accurately known, then a simple method can be used to determine the step size. Provided that the sample holder on the walker's sapphire rod is well away from the tube scanner, the walker can be moved by an auto-approach forwards or backwards for a period of time sufficient for the distance moved to be observed without difficulty. The distance that the sample holder has moved can then be measured either using a ruler or by comparison with reference points on the STM head, and the number of steps taken to move that distance noted from the control unit. From these figures, a value for the average step size can be calculated.

If the STM is in UHV or inserted in a cryostat and no longer visible, then the following procedure for measuring the step size may prove useful. The Z voltage being sent to the tube scanner should be measured with an oscilloscope either by connecting it to a low voltage output proportional to it or by using a 10:1 probe connected to the wires leading to the tube scanner. If the tube scanner configuration being used combines the Z voltage signal with that of the X and Y deflections at each quadrant (i.e. $Z \pm X$, $Z \pm Y$ mode of operation) then the voltages at two opposite quadrants must be measured and half the value of their sum taken as the Z voltage itself. However, if the X and Y deflections can be set to zero in the software (typically setting the

X and Y scan position to zero and the scan area to zero will achieve this) then measuring the voltage on one quadrant is sufficient to determine the amplitude of the Z signal.

1. Bring the tip into tunnelling on a sample. Adjust the position of the sample with the piezowalker (retracting the tip before each movement) until the Z voltage, V_o , is close to 0 V.
2. Withdraw the tip and retract the sample by 10 steps using the piezowalker (generally the tip will still be within tunnelling range even after taking 10 steps). Bring the tip forward again and measure the value of the new Z voltage, V_b . Note that this value will change over time due to piezo creep in the tube scanner, and it is therefore useful to take only the initial value after each change in the tube scanner extension.
3. Withdraw the tip and bring the sample 10 steps closer to the tip. Bring the tip forward again and note the Z voltage, V_f . Note that in general V_f will not be the same as V_o because the step sizes in opposite directions are not equal.

The ratio of forward (S_f) to backward step size (S_b) is then given by the difference in the voltages, as shown in the following equation:

$$\frac{S_f}{S_b} = \frac{V_b - V_f}{V_b - V_o} \quad (3.1)$$

This ratio should ideally be close to 1, but will in practice be between 0.6 and 0.8. Once the Z sensitivity of the tube scanner is known, and the high voltages applied to the tube scanner have been measured as above, the

Table 3.2: Measured Piezo Walker Step Sizes

<i>STM Name</i>	Applied V_{pp} (V)	<i>Foward</i> <i>step size</i> (nm)	<i>Backward</i> <i>step size</i> (nm)	<i>Step size</i> <i>ratio</i>
RT STM	160	35	50	0.7
LT STM	160	52	75	0.7
Ti RT STM	250	29	49	0.6

physical step height can be determined from the values recorded in the above procedure. The values determined for the walkers used in several STM that are used in this project are given in Table 3.2. As can be seen in this table, the step size of the LT STM when operated at room temperature is much greater than the other piezowalkers in order to ensure that the step size is adequate at low temperatures.

3.4.2 Tube scanner

The resonance frequencies of the tube scanner both in the vertical (Z) direction and in the lateral (X, Y) directions determine the maximum scanning rate at which the STM can operate. It is the X and Y scan speeds which are varied regularly during an STM session, and the rate at which the Z height changes is determined by the sample topography. During a normal scan the X scan speed is generally much faster than the Y scan speed.

The frequency at which the tube scanner scans in the X or Y direction should be significantly below the value of the corresponding resonance

frequency. Formulas for calculating the resonance frequencies of the tube scanner can be found in the literature [28,61], however the accuracy of these formulas in practice has not been confirmed, and their use in determining quantitative values of the tube scanner piezoelectric coefficients can be inconsistent [62].

Basic tests

In order to test the wiring leading to the tube scanner, it is useful to measure the capacitance between the quadrants of the tube scanner. This can be conveniently and accurately measured using a multimeter such as a Textronix DMM 912 or Fluke 83 III. The measurement can be made between the signal wires of the BNCs leading to the tube scanner. The capacitance of the wires (which is typically 50 picofarads per metre) is a lot less than the capacitance between the quadrants (which is of the order of nanofarads). For example, the capacitance between each quadrant on the tube scanners in the LT STM and Ti RT STM and the ground is typically 4 nF. The measured capacitance between two quadrants was found to be between 2 nF and 2.5 nF when measured at the air-side of the electrical feed-through leading to them.

Resonance frequencies

The procedure outlined below gives a useful indication of whether the tube scanner wiring is functioning, and also enables the measurement of the tube scanner's resonance frequencies. This test uses the inverse piezo effect [28] to check whether all four quadrants of the tube scanner are connected correctly. This is achieved by applying a sinusoidal voltage to one quadrant in order

to make it extend and contract. This deforms the opposite quadrant and a voltage change should be detected across it. In addition the adjacent piezo quadrants are capacitively coupled to the excited quadrant, and a cross-talk signal can also be detected on them. This cross-talk signal is distinct from a leakage signal as it is caused by capacitive coupling, whereas a leakage signal is caused by resistive coupling. The presence of a tip holder in the tube scanner changes the resonance frequency. As the mass and length of both tips and tip holders vary, it is best to do the measurements without a tip holder in place in order to determine the intrinsic resonance frequencies of the tube scanner.

In the STMs used in this project, only one of the BNCs on the cables leading to the tube scanner feedthrough has its shielding braid connected to the tube scanner ground. It is therefore important that this BNC should be grounded at all times. In addition, if the other cables are not grounded, extra noise may be brought into the region of the tube scanner through those wires. It is therefore necessary to ground the shields of all of the BNCs leading to the tube scanner. This can be done conveniently by connecting them to an oscilloscope.

A summary of the procedure is given below:

1. Using a function generator, apply a sinusoidal voltage of amplitude 2 V peak-to-peak to the Z+X quadrant.
2. While varying the frequency of the applied signal, use an oscilloscope to monitor both it and the corresponding signal in the Z-X quadrant.
3. Find the lowest resonance frequency of the Z+X quadrant by identifying the frequency at which the Z-X signal is largest.

<i>STM Name</i>	<i>Quadrants</i>	<i>Resonance frequency (kHz)</i>	<i>V_{pp} on opposite quadrant (mV)</i>
LT STM	$Z \pm X$	1.67	≈ 100
	$Z \pm Y$	2.09	≈ 1000
Ti RT STM	$Z \pm X$	1.53	≈ 380
	$Z \pm Y$	1.56	≈ 70

Table 3.3: Measured Tube Scanner Resonance Frequencies

4. Repeat this procedure for the other three quadrants.

The resonance frequencies measured using this procedure are shown in Table 3.3. It can be seen from that table that the resonance frequencies are typically around 1.5 kHz and that at those frequencies the pickup on the opposite quadrants is significant. It is also interesting to note that there is a significant difference between the amplitude of the voltage measured on the X and Y quadrants. The reasons for this are unclear as these quadrants should have similar properties. It is possible that as the wires leading to the STM head follow slightly different routes that some of them are closer to one another and lead to a greater pickup signal. It is also possible that some extra conducting glue might be present close to the electrodes of some of the quadrants and that this may influence the measured variations.

This procedure can also be used to test whether any of the scanner wires have become detached. This technique would be especially useful in the case of the STM head being cooled in a cryostat where the wires leading to the piezoceramic tube scanner would not be visible. If a wire has become detached then it will pick up a smaller signal from its neighbouring electrode than its

equivalent on the opposite side of the tube scanner. For example, if the $Z+X$ wire has become detached then it would pick up a smaller signal than the $Z-X$ wire when a sinusoidal signal is applied to either of the $Z\pm Y$ electrodes.

3.4.3 Pre-amplifier

A pre-amplifier is used to amplify and convert the tunnel current into a voltage that is then measured by the control unit. This chip (usually a Burr-Brown OPA-111SM operation amplifier in the STMs used in this project) is often located adjacent to the STM head [25, 42, 45]. It may become damaged during the routine bakeouts necessary to achieve ultra high vacuum after the system has been up at air. It is possible that during the bakeout, the operational amplifier becomes damaged at the moment when the ion pump is switched on. In some cases, there is a discharge in the vacuum chamber during the switching on of the pump. This discharge can be seen through a viewport as a blue glow inside the chamber and possibly connects the tip and therefore the input of the amplifier to the high voltage of the ion pump.

It is useful to systematically check whether the pre-amplifier is functioning correctly. A useful method to do this is to start an auto-approach and monitor the pickup on the I_t signal (neither a tip or sample need be in the STM for this test to work). During an auto-approach two distinct waveforms can be seen on the normally flat tunnel current signal. One is caused by the sudden voltage change in the tube scanner coinciding with the fast retraction of the tip. The other occurs approximately 14 ms later when the walker takes a step and is due to the high voltage signal being sent to the walker piezos. Note that the presence of a filter box on the I_t signal cable will change the shape

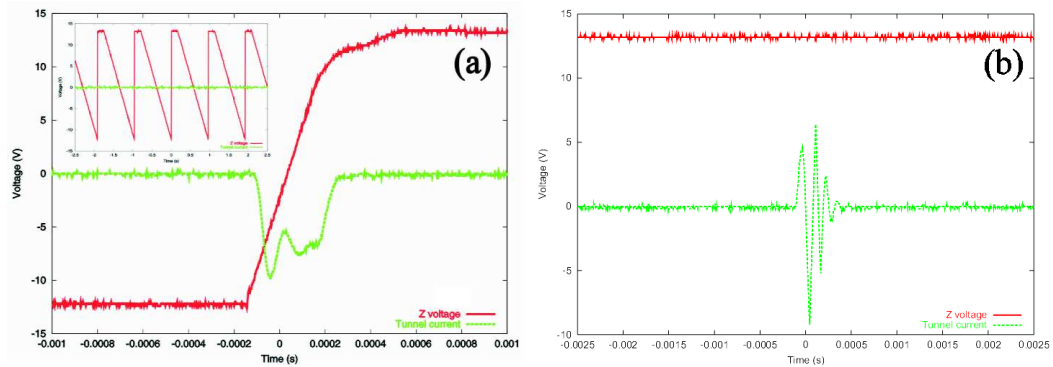


Figure 3.2: The pickup measured on the tunnel current signal. (a) The change in the tunnel current signal as the tube scanner is retracted quickly. The inset shows the shape of the ramping sawtooth-like voltage applied to the tube scanner during the autoapproach. (b) This graph shows the pick-up signal tunnel current (green) approximately 14 ms after the fast retraction of the tube scanner.

of the observed waveform.

The Scala electronics have been adapted as part of this project to reduce the rate of auto-approach to 2 Hz, i.e. two steps a second, ensuring that the tip is not crashed into the sample by rapid movement of the piezowalker. The last few iterations of the auto-approach also indicate whether the auto-approach routine itself is functioning correctly and whether the correct voltage polarity has been chosen for the Z tube scanner signal. If the tip consistently crashes into the sample on the last iteration of the auto-approach procedure then this indicates that the wrong polarity has been chosen for the scanner Z voltage in the controller. The STMs used in this project are what are referred to as “negative polarity” by Omicron, the manufacturers of the control unit. This means that the tip-to-sample distance decreases when the voltage applied to

the tube scanner is increased.

The waveforms shown on the oscilloscope during the auto-approach should be similar to the ones shown in Figure 3.2 which were recorded on the Macor RT STM. The inset in Figure 3.2 shows the oscilloscope trace of the repeated slow decreasing ramp of the Z voltage as the tube extends looking for the sample. The first pickup on I_t (shown in Figure 3.2a) is due to the fast retraction of the tube scanner. There is another pickup on the I_t signal after about 14 ms corresponding to a coarse step taken by the walker after each unsuccessful attempt to enter tunnelling by extending the tube scanner. This pickup signal is shown in Figure 3.2b. Modifications to the design of the wiring in the STM should minimise the amplitude of these pick-up signals, although their presence is useful in confirming that the pre-amplifier is connected correctly to the tunnelling current.

Chapter 4

Iron Films on Molybdenum

The direction of magnetization in thin films of iron has been shown to be very sensitive to the presence of contaminants, including those in the residual gas [63,64]. As the magnetization states in the film are also sensitive to dislocations in the epitaxial film [65,66], it is important to ensure that the surface of the molybdenum substrate is regular and free of impurities before the deposition of iron. This is achieved by the repeated annealing of the Mo(110) substrate at high temperatures for short time intervals. This procedure, known as “flash-annealing” or “flashing”, typically heats the sample to approximately 2,300 K for between 5 and 15 seconds. This leads to the desorption of adsorbates from the surface, including the Fe that may be present from previous depositions.

The Fe was deposited using an e-beam evaporator that was designed and built in-house. The thickness of the film deposited was measured with a commercial quartz crystal deposition monitor, as described in the Experimental chapter and elsewhere [48]. This thickness measurement is given in units of pseudomorphic monolayer equivalents (ML).

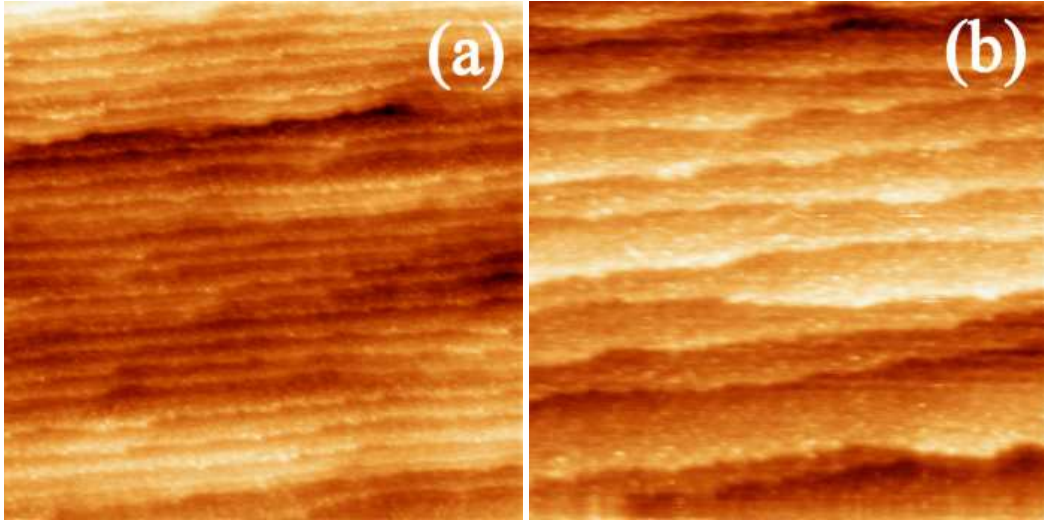


Figure 4.1: Images of the Mo(110) substrate before subsequent flashing led to an improved surface quality, as confirmed by AES, LEED and STM. (a) A $200\text{nm} \times 200\text{nm}$ scan showing the uneven nature of the $[1\bar{1}1]$ step edges. (b) A $100\text{nm} \times 100\text{nm}$ image showing occasional double steps. Tip = W, $V_{bias} = 0.1\text{ V}$, $I_t = 0.1\text{ nA}$ in both cases.

4.1 Mo(110) Substrate

In order to successfully deposit a pure thin film of Fe, the Mo(110) substrate must be carefully prepared. In these experiments, this preparation took the form of flash annealing which led to the rapid desorption of contaminants from the sample surface as well as the removal of any iron remaining from previous depositions. The stepped nature of this vicinal Mo(110) surface (which has been miscut from the plane by approximately 5° [48]) can clearly be seen in Figure 4.1a.

In this case, the flash-annealing process has not yet completely removed the contaminants. The step edges are irregular and do not form straight

lines, although the general step edge orientation is along the $[\bar{1}\bar{1}1]$ direction. A closer look at the sample surface (shown in Figure 4.1b) also show steps where very narrow terraces have formed. Contaminant particles can also be seen on the sample surface. These are most likely either iron from previous depositions or impurities that were present in the residual gas in the UHV chamber. Subsequent flash-annealing stages led to an improvement in the surface quality, as confirmed by AES, LEED and STM.

4.2 1.2 ML Fe on Mo(110) at 315 K

The morphology of thin iron films depends on several parameters, including the substrate temperature and deposition rate. The film described here consisted of a 1.2 ML thick iron film deposited on a substrate that was slightly above room temperature at 315 K. The deposition rate was $0.6 \text{ ML}\cdot\text{min}^{-1}$. The Auger spectrum of this sample showed the presence of both oxygen and iron, indicating that an iron oxide had formed on the sample surface during the deposition. The LEED pattern obtained on this surface was consistent with a $p(2 \times 2)$ reconstruction of the sample surface.

Two separate STM scans showing the structure of a 1.2 ML thick film deposited close to room temperature at 315 K are reproduced in Figure 4.2. As can be seen in the large area scan of Figure 4.2a, the growth mode is uniform across this area of the sample. Closer inspection of the sample surface (shown in Figure 4.2b after 2D-FFT processing) shows the nature of the growth in greater detail. There appears to be growth by the step-flow mechanism out from the step edges, as well as a degree of island nucleation away from the edges on the molybdenum terraces. As the amount of Fe

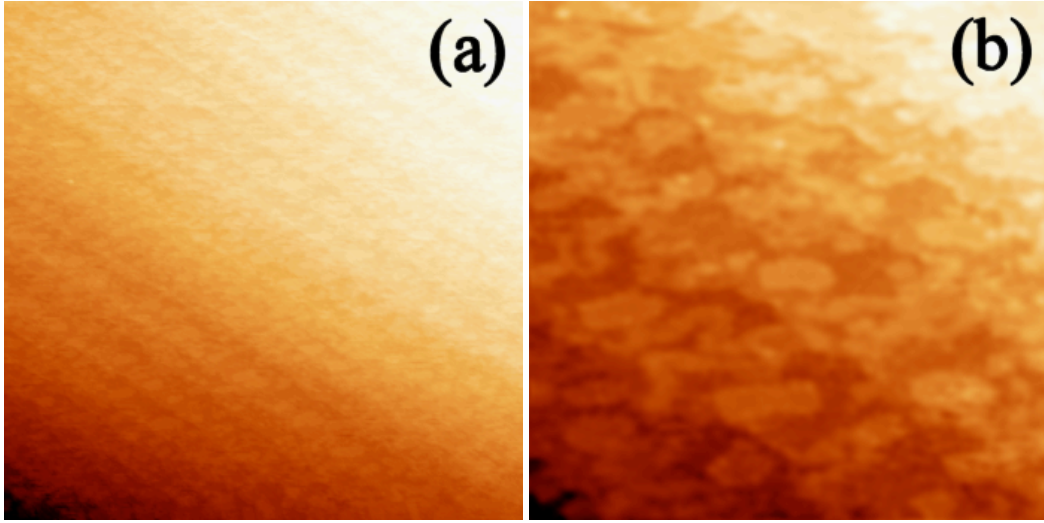


Figure 4.2: These images show a 1.2 ML Fe film grown on Mo(110) at 315 K. (a) This $200\text{nm} \times 200\text{nm}$ scan shows the uniformity of the sample. $V_{bias} = 0.03$ V, $I_t = 0.1$ nA. (b) This small area ($50\text{nm} \times 50\text{nm}$) scan has been filtered using a FFT process to improve the image quality and shows the combination of step-flow growth and island nucleation. $V_{bias} = 0.1$ V, $I_t = 0.1$ nA. Tip = W in both cases.

deposited corresponds to approximately a monolayer of iron, it appears that the bare molybdenum substrate can also be seen between regions covered by iron. It is interesting to compare this film with a similar film grown during a previous set of experiments (Film C in Reference [48]) at a slightly slower deposition rate of $0.443\text{ML}\cdot\text{min}^{-1}$. In that case there was almost complete closure of the first pseudomorphic layer before nucleation of the second layer began. In the film studied here, the first layer does not appear to be closed completely although a significant amount of the second layer has grown.

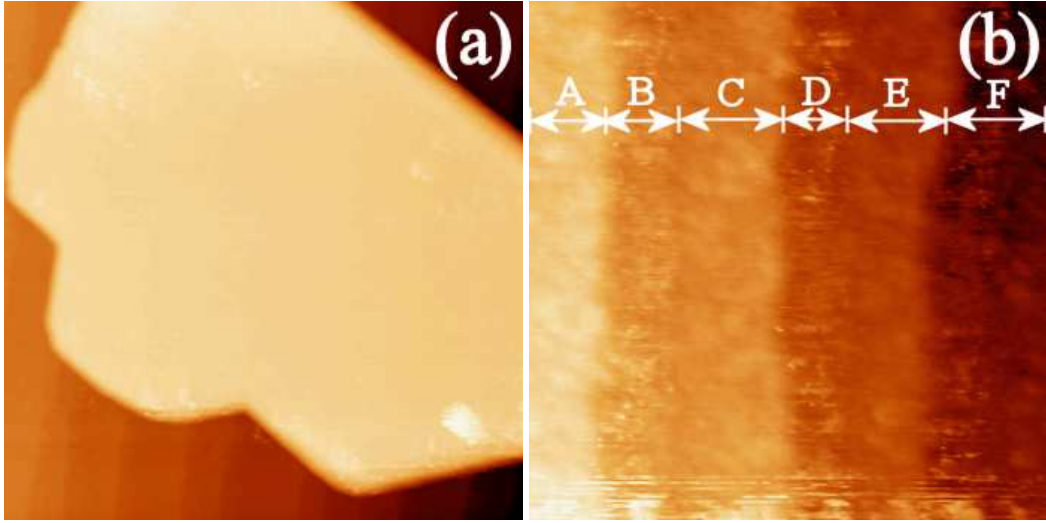


Figure 4.3: STM results on a 3.6 ML Fe film grown on Mo(110) at 800 K. (a) A large Fe island can be seen in this $200\text{nm} \times 200\text{nm}$ image. $V_{bias} = 0.1\text{V}$, $I_t = 0.1\text{nA}$. (b) A $49\text{nm} \times 49\text{nm}$ scan of the area between the large Fe islands. Unusually, the surface roughness varies across each terrace. $V_{bias} = 0.03\text{ V}$, $I_t = 0.1\text{ nA}$. Tip = MnNi in both cases.

4.3 3.6 ML Fe on Mo(110) at 800 K

A significant change in the growth mode is observed when a thicker iron film is deposited at a higher temperature. In this case, a 3.6 ML thick film was deposited on a substrate that was heated to 800 K in a resistive heater during the deposition. The deposition rate was similar to the one used in the experiment described above, and was approximately $0.45\text{ ML}\cdot\text{min}^{-1}$.

The iron islands in this case are very large, with a width and length of approximately 200 nm as can be seen in Figure 4.3a. A 3D representation of this image (Figure 4.4) shows the wedge shaped nature of the island clearly. These images were scanned with an antiferromagnetic MnNi tip. As discussed

in detail elsewhere [48,67,68], iron films deposited on molybdenum at elevated temperatures apparently grow in the Stranski-Krastanov (SK) growth mode, where the islands form on an initial iron layer that has grown pseudomorphically on the molybdenum substrate. This also appears to be the case here, as the smaller area scan of the area between large islands shown in Figure 4.3b does not appear to be of exposed molybdenum terraces.

This image shows several interesting features when compared with similar sized scans of the 1.2 ML film. The width of the terraces is much larger in this case, indicating that the formation of the iron layer has changed the topography of the surface. The iron layers have grown in such a way as to reduce the number of steps. In addition, the surface roughness varies across each terrace, with the left-hand side of each terrace having a different structure to the right-hand side. The terraces have been labelled in Figure 4.3b. It appears that terraces A, C and E have one type of structure or roughness and that terraces B, D and F have another type of structure. These results suggest that the lower iron layer has various thicknesses and that in some regions a monolayer of iron covers a molybdenum terrace while on the adjacent step down terrace a double layer of iron has formed. This structure is indicated schematically in Figure 2.1b. It is likely that terraces A, C and E are double layers and that B, D and F are single layers of iron, and that Fe-nanostripe arrays have formed underneath and between the large islands.

The differences observed in the STM images could be related to the differences in crystal structure of those parts of the terrace due to the transition from monolayer to double layer. The variations seen could also be due to the

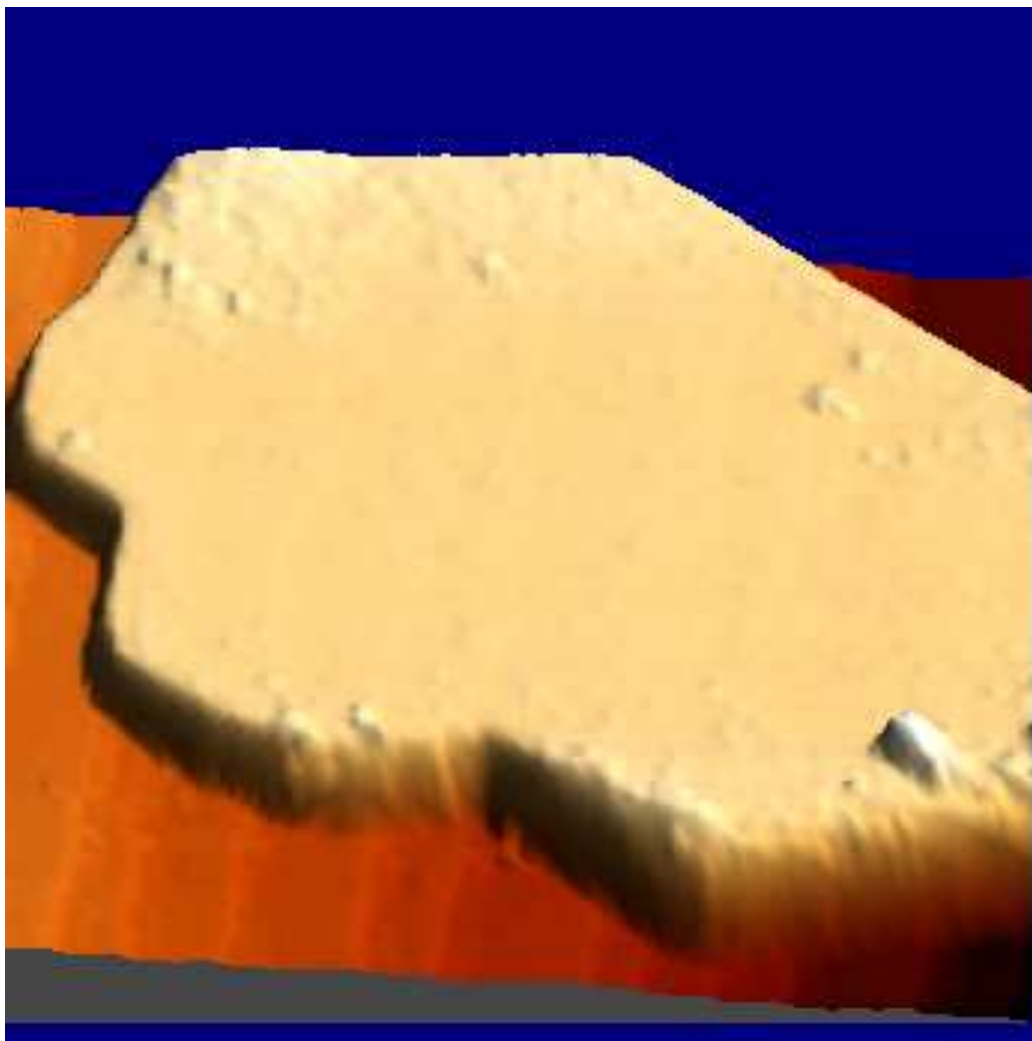


Figure 4.4: A 3-dimensional representation of the STM data shown in Figure 4.3a. The wedge-shaped nature of the large Fe island can be seen. $V_{bias} = 0.1$ V, $I_t = 0.1$ nA. Tip = MnNi.

MnNi tip imaging the difference in the magnetization direction of the iron film [69–71]. Note that these images should be compared with those from the previous experiment with care as they were scanned using different STM controllers. In order to test whether the effect seen is magnetic, it would be useful in future work to grow a similar film and study it with a magnetically sensitive STM tip both with and without a magnetic field applied to it [34]. If a change was noticed between the images then it is likely that this change was magnetic effect in origin.

These experiments on the growth of iron films on a stepped molybdenum substrate have demonstrated the importance of substrate preparation and characterisation prior to iron deposition. The 1.2 ML film deposited here showed a mixture of Frank-van der Merwe and Volmer-Weber growth, while the the 3.6 ML film appeared to form by Stranski-Krastanov growth with wedge-shaped islands forming on top of iron layers. The area between the large wedge-shaped iron islands formed during the growth of the 3.6 ML film exhibited anomolous topographic effects. These effects are possibly related to the variation in crystal structure between double and mono-layers of iron. It also possible that the antiferromagnetic MnNi tip used here was imaging the predicted variation in magnetic properties between these layers, and further experiments with an applied magnetic field could confirm whether this is the case.

Chapter 5

Unpolished Magnetite Surface

Research on Magnetite (Fe_3O_4) continues to provide interesting results which are becoming increasingly relevant to recording technologies based on magnetism. For the purposes of this project it was decided initially to investigate the (001) surface of artificially grown Fe_3O_4 single crystals. These crystals were grown by the group of Professor Honig in Purdue University, USA by the so-called skull melting technique, as described in Reference [40]. These single crystals were then cut into slices approximately 1 mm thick oriented in the (001) plane with an accuracy of approximately 0.5 angular degrees by the group of Dr Bozhko in the Institute of Solid State Physics, RAS, Moscow, Russia. The slice of magnetite used as a sample in this set of experiments was referred to as “Hru1” on the protocol sheets and laboratory notes.

Once cut, one side of the sample was polished first with 0.3 μm and then with 0.05 μm Al_2O_3 powder, while the other side was left in its rough “as cut” state. Some of the single crystals supplied contained macroscopic defects which limited the accuracy of the polishing. Such dislocations are common in crystals, and iron oxides may also be twinned, where two slightly

different orientations of the crystal are present in one sample [23]. In order to study the effects of surface roughness on the magnetite sample, it was decided to investigate both the polished and unpolished side of the sample. The unpolished face of the sample was studied first. Before being loaded into the UHV system, the sample was cleaned by placing it on a lint-free tissue in a petri dish, submerging it in ethanol and then placing both sample and petri dish in an ultrasonic bath.

5.1 AES analysis

Auger Electron Spectroscopy (AES) was used to study the chemical composition of the sample surface after it was loaded into the UHV system. A representative set of the spectra recorded are shown in Figure 5.1.

Various primary beam energies were used during this set of experiments in order to distinguish Auger peaks from peaks due to primary electrons which have lost a discrete amount of energy through the ionization of core levels. As outlined in Reference [47], any peak that moves as a function of the primary beam energy is not an Auger peak. Using the method described in References [26,47], the AES spectra have been used to determine approximate values for the atomic concentrations of elements at the sample surface, and these are tabulated in Table 5.1.

When it was first placed in the UHV system only a large carbon peak and a small oxygen peak were significantly above the background noise level as can be seen in Figure 5.1a. These peaks correspond to a carbon atomic concentration of $C_C = 0.94$, and an oxygen atomic concentration of $C_O = 0.06$. One possible source of this large amount of carbon is the ethanol in

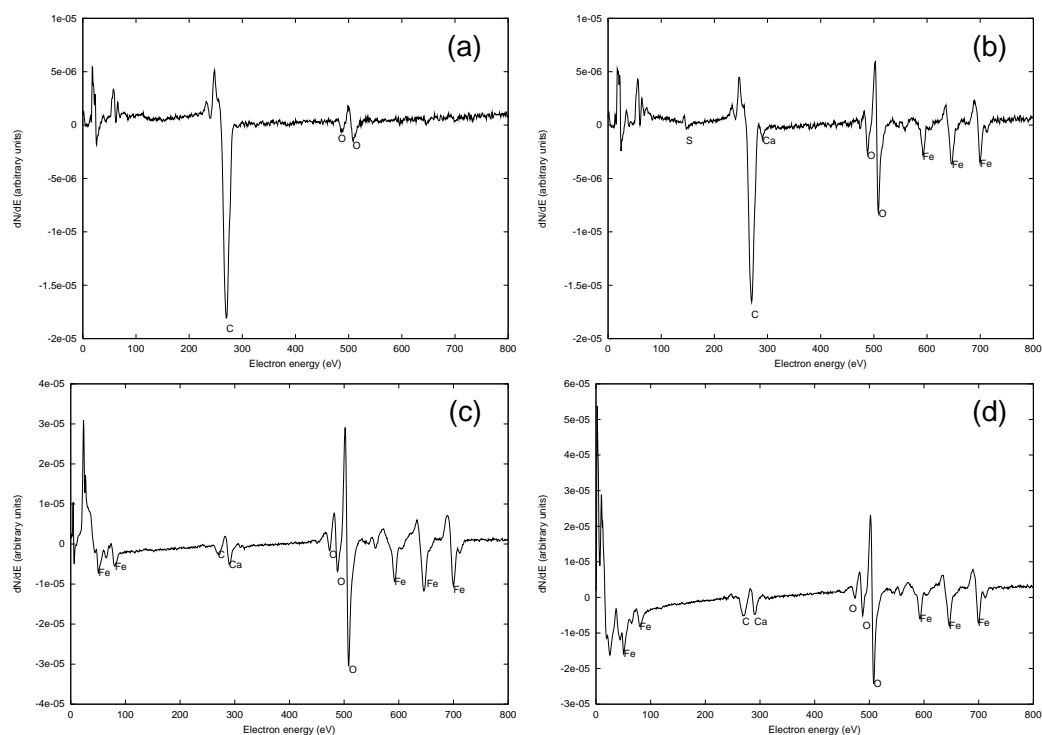


Figure 5.1: A representative set of AES spectra showing the chemical composition of the sample surface after sequential anneal stages. The primary beam energy (E_B) was varied to distinguish Auger peaks from artifacts due to primary electrons [47]. (a) Before annealing. $E_B = 3$ keV. (b) After a 4 hour anneal at 900 ± 20 K. A small sulphur peak can be seen. $E_B = 3$ keV. (c) After annealing for 126 hours at 900 ± 20 K followed by 57 hours at 950 ± 20 K. $E_B = 2$ keV. (d) After 60 hours of annealing at 950 ± 20 K. $E_B = 1.6$ keV.

Table 5.1: Surface Atomic Concentrations of Unpolished Magnetite

<i>Anneal time (hours)</i>	<i>Anneal temp. (K)</i>	<i>C</i>	<i>Ca</i>	<i>O</i>	<i>Fe</i>	<i>S</i>
0	–	0.94	0.00	0.06	0.00	0.00
4	900 ± 20 K	0.61	0.02	0.17	0.19	0.01
126 + 57	900 ± 20 K then 950 ± 20 K	0.04	0.07	0.52	0.37	0.00
60	950 ± 20 K	0.10	0.07	0.46	0.37	0.00

which the sample was cleaned. It has, however, been noted previously that even samples which were not washed in ethanol but were exposed to air show a significant level of carbon contamination [21]. This indicates that air-borne hydrocarbons also adsorb onto the surface.

Annealing the sample for 4 hours at a temperature of 900 ± 20 K led to a temporary increase in the chamber pressure to 10^{-8} torr before it stabilized at a pressure in the mid 10^{-10} torr range. This indicates that contaminants were desorbing from the sample surface during the annealing. The Auger spectrum after this annealing stage (Figure 5.1b) shows a reduced carbon level of $C_C = 0.62$ while the oxygen and high energy iron peaks are now clearly visible, with $C_O = 0.17$ and $C_{Fe} = 0.19$. A small sulphur peak corresponding to $C_S = 0.01$ appears in this AES spectrum. In addition, a small calcium peak indicating $C_{Ca} = 0.02$ can be seen, indicating that calcium has diffused from the bulk

of the crystal to the surface.

Further annealing stages with a total anneal time of 126 hours at 900 ± 20 K did not result in a significant decrease in the level of the carbon present on the surface. However, annealing stages at a higher temperature of 950 ± 20 K for a total of 57 hours did however lead to the carbon concentration, $C_C = 0.04$, decreasing to less than the calcium level, $C_{Ca} = 0.07$, as shown in Figure 5.1c. Interestingly, after annealing at this temperature for an additional 60 hours the amplitude of the carbon level increases once again to $C_C = 0.10$, and is slightly greater than the calcium concentration of $C_{Ca} = 0.07$, as the spectrum in Figure 5.1d shows. As this is against the general trend of the annealing stages, it is probable that the initial annealing stage causes carbon which has adsorbed onto the surface to desorb from the surface. The subsequent increase in the level of carbon after annealing is probably due to carbon diffusing from the bulk of the sample to the surface.

From these experimental AES results, it appears that the annealing temperature of 950 ± 20 K is high enough to rapidly desorb the carbon on the surface. However, this temperature also promotes the diffusion of impurities from the bulk of the crystal. If experimental conditions are such that long annealing times of the order of hundreds of hours are practical, then the lower annealing temperature of 900 ± 20 K could be used to avoid the diffusion of bulk contaminants such as Ca while gradually decreasing the amount of carbon at the surface. The technique of ion bombardment could also be used to remove contaminants, however this technique was not used in this study in order to avoid significant changes to the sample surface topography.

5.2 LEED patterns

The crystal structure of the sample surface was studied with Low Energy Electron Diffraction (LEED). When the sample was first loaded into the vacuum chamber, no diffraction spots were visible with LEED, indicating that the sample surface was disordered. After a series of anneal stages with a total anneal time of 24 hours at 900 ± 20 K a faint pattern was observed. There has been some discussion in the literature about the appropriate notation for describing the crystal structure of the magnetite surface in both its reconstructed and unreconstructed states. A clear overview of this debate is given in [72]. The LEED pattern observed is consistent with the reciprocal lattice of the primitive surface unit cell with dimensions of $6 \text{ \AA} \times 6 \text{ \AA}$ [27] and will therefore be referred to as (1×1) . Note that this primitive surface unit cell is different from the projected bulk unit cell, which has dimensions of $8.4 \text{ \AA} \times 8.4 \text{ \AA}$. This is consistent with an unreconstructed surface, although the blurred nature of the spots indicates a poor overall structuring of the sample surface. Apart from one LEED session where no pattern at all was observed, the (1×1) pattern remained visible but faint during subsequent anneal stages.

It is interesting to note that a (1×1) pattern is not expected on clean Fe_3O_4 as the (001) surface is polar and has an imbalance of positively and negatively charged ions. Such polar surfaces of highly ionic crystals therefore are highly unstable and normally reconstruct [26, 27]. It is likely therefore that the presence of contaminants on the magnetite surface of this sample is stabilizing the surface. A similar pattern was observed by Anderson et al [27] and they attributed it to the massive segregation of a contaminant (Mg in

their case) to the surface, leading to an overlayer of that impurity. It is likely that an overlayer partly composed of carbon and/or calcium is present on this sample.

5.3 STM images

The STM images of the sample (four of which are shown in Figure 5.2) confirm that the unpolished side of the sample is very rough and therefore unsuitable for STM experiments. Before annealing, long depressions were present on the surface as can be seen in Figure 5.2a and in 3D form in Figure 5.3. These depressions were linear and quite long, continuing for distances over $1\mu\text{m}$. They were approximately 6 nm deep and 100 nm wide. It is possible that these features are scratches resulting from the cutting of the crystal into slices.

After annealing the sample for 4 hours at a temperature of 900 ± 20 K, the topography of the sample surface changed, as shown in Figure 5.2b. No scratches were observed in any of the areas scanned during the STM session after the anneal was completed, although some large features were present. These features take the form of protrusions on the surface which are approximately 20 nm high while the flatter areas of the sample contain some depressions. It is possible that the annealing stage caused large mass transport effects in the sample and that the magnetite surface was effectively regrown in UHV during the anneal.

Smaller area scans of the surface show the presence of small clusters. Before annealing, the clusters were quite large as can be seen in Figure 5.2c. By comparing the STM images with Auger spectra taken after the same

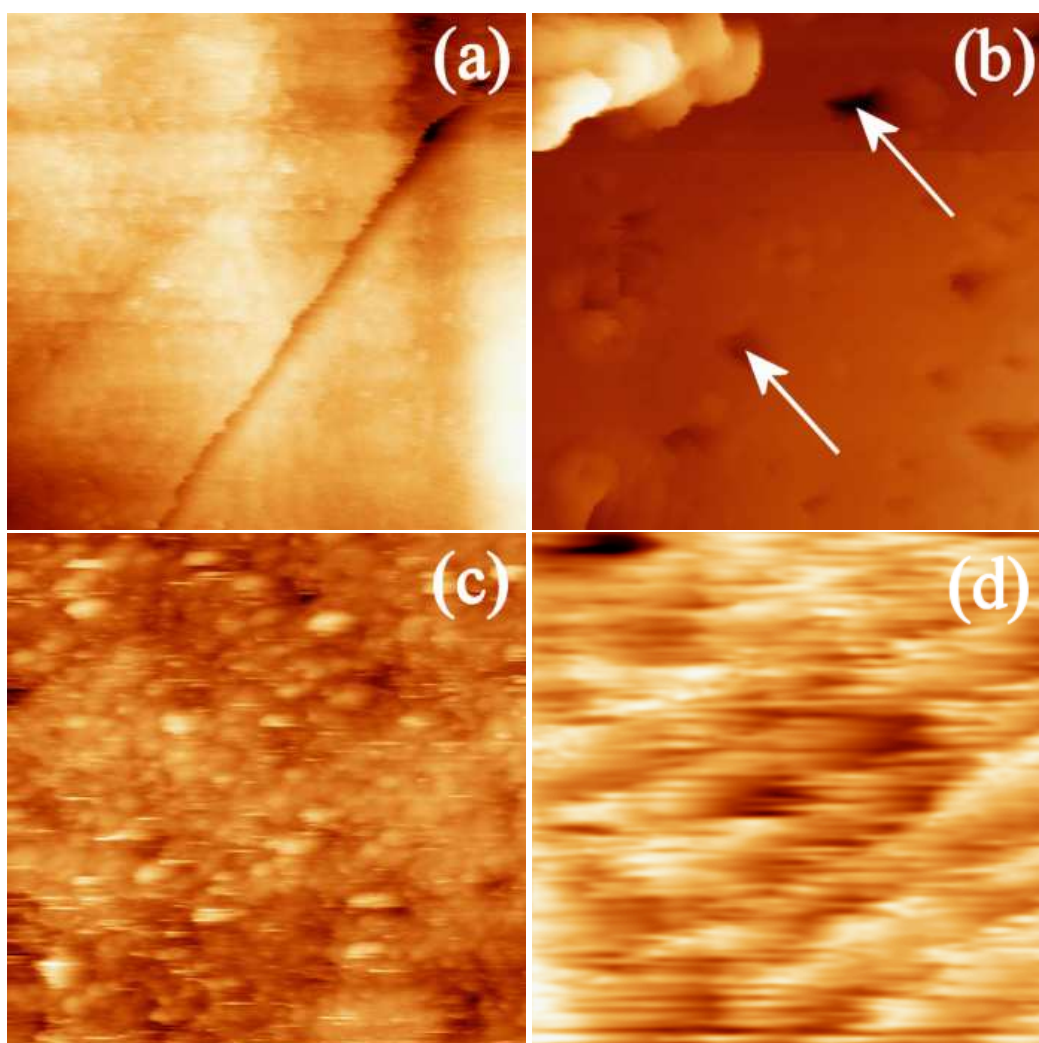


Figure 5.2: STM images showing the structure of the unpolished Fe_3O_4 (001) sample surface. (a) Before annealing the sample appears very rough and linear depressions (possibly scratches) are visible in this $1\mu m \times 1\mu m$ scan. $V_{bias} = 1$ V, $I_t = 0.5$ nA (b) Holes (indicated by arrows in the figure) appear in this $1\mu m \times 1\mu m$ image after annealing for 4 hours at 900 ± 20 K, and although the height variations on the surface have decreased, large features still remain. $V_{bias} = 0.1$ V, $I_t = 1$ nA. (c) A $50nm \times 50nm$ image showing the presence of clusters before the sample was annealed. $V_{bias} = 1$ V, $I_t = 0.5$ nA. (d) After extensive annealing, rows were seen on the sample surface as shown in this $5nm \times 5nm$ scan. $V_{bias} = 1$ V, $I_t = 0.1$ nA. Tip = W in all cases.

anneal stages it would appear that these clusters can be attributed to the presence of carbon on the surface.

After a lengthy sequence of annealing stages, it was however possible to image regularly spaced rows on the sample surface. As resonance of the tube scanner can lead to the presence of rows in STM images, care was taken to confirm that this was not the case by changing various scanning parameters. These rows are shown in Figure 5.2d. which was processed with a 2D-FFT filter in order to emphasise the periodicity of the rows and to reduce the smearing present in the images. These rows were present in the original unprocessed image and were not an artifact caused by the image processing algorithm.

By using line profiles to measure the periodicity of the rows in the direction perpendicular to them it was found that they are spaced by 7 ± 1 Å. It is possible that these rows are octahedral Fe ions in rows at the surface. Such rows would be separated by a distance of 6 Å. However, as the corresponding Auger spectrum shows the presence of both carbon and calcium on the sample surface, it is more likely that the atoms imaged in the rows are impurities. These contaminants possibly preferentially occupy certain bridge sites on the Fe_3O_4 surface.

The large height variations across the sample made STM scans difficult. The speed of the feedback loop had to be maintained at a relatively high value in order for the tip to follow the large variations in the topography of the sample. The clusters that were present on the sample during most of the scanning sessions also made small area scans quite difficult as they moved with the tip and led to a smearing of the images.

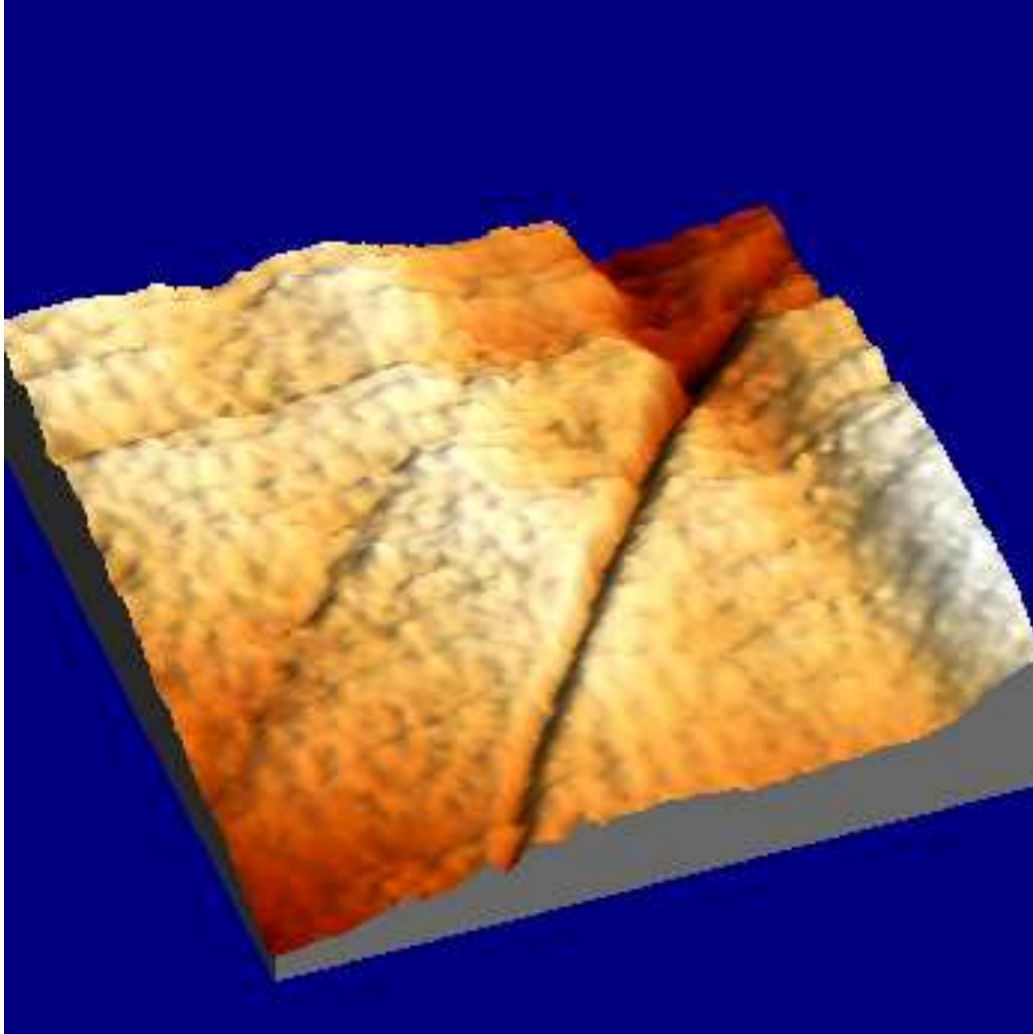


Figure 5.3: A 3-dimensional representation of the $1000nm \times 1000nm$ scan shown in Figure 5.2a. The roughness and scratches on the surface can be clearly seen. $V_{bias} = 1V, I_t = 0.1nA$

From these results, it is apparent that the surface topography and composition changes significantly as a function of anneal time. It is unclear whether the annealing process causes the large-scale movement of Fe and O atoms on the surface or whether all the topography variation is caused by the movement of C and other adsorbates such as water. It appears that a combination of both processes takes place. Large movements of all the elements at the surface cause the scratches initially present to be “smoothed out”. The desorption of the carbon overlayer on the surface then allows the underlying cubic crystal structure of the magnetite to manifest itself in the form of four-sided holes on the surface.

Chapter 6

Polished Magnetite Surface

The large variations in the surface height and the persistence of the carbon contamination made STM imaging and analysis of the unpolished side of the magnetite sample difficult. In order to investigate the polished face of the sample, it was removed from the UHV system, turned over to expose the mechanically polished side and then re-inserted into the vacuum chamber. The sample was not re-cleaned with organic solvents while it was in air. Due to the presence of macroscopic defects in the sample, the accuracy of the sample polishing in the (001) plane varied, and a small area of this sample has been polished at a different angle to the rest of the sample face. It should be noted that the polished side of the sample was annealed face down for a large number of hours while the rough side of the sample was being investigated. This could potentially lead to the diffusion of impurities from the sample holder into the sample itself, although extensive studies with AES failed to find any trace of contamination by the materials used to make the sample caps (Mo and Ta).

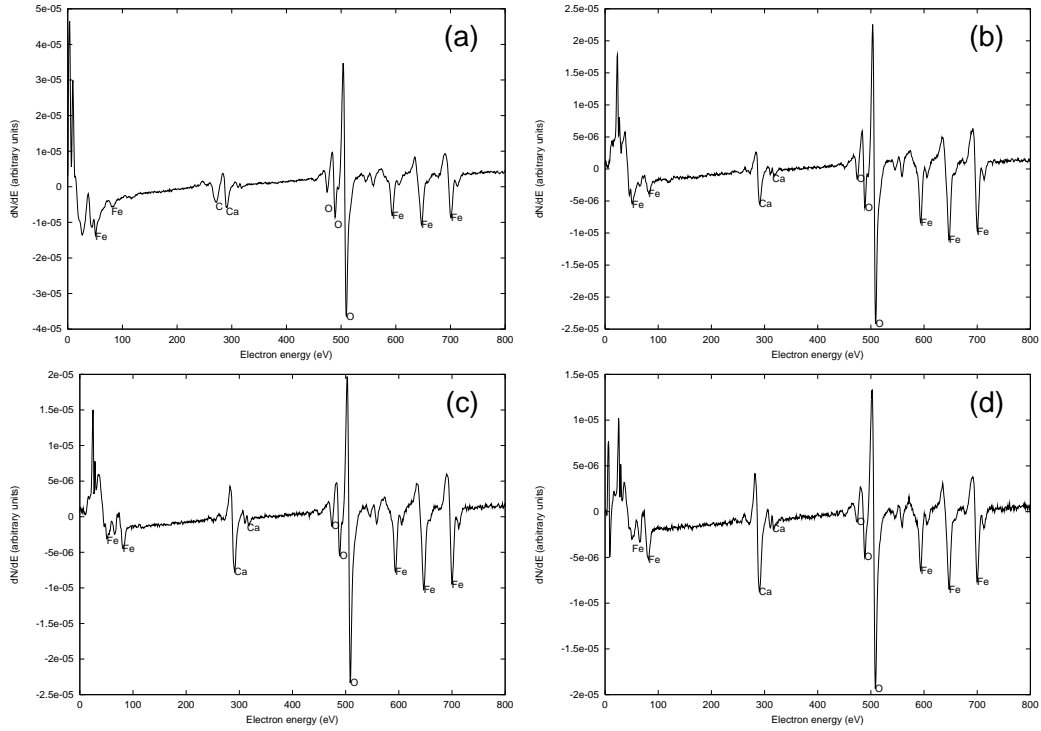


Figure 6.1: AES spectra showing the chemical composition of the polished magnetite surface after various anneal stages. (a) Before annealing with the polished face exposed, $E_B = 1.6$ keV. (b) After a 15 hour anneal at 950 ± 20 K. $E_B = 2$ keV. (c) After a 60 hour anneal at 950 ± 20 K. $E_B = 2$ keV. (d) After a 37 hour anneal at 950 ± 20 K. $E_B = 2$ keV.

6.1 AES analysis

The AES spectra of the sample after it was returned to the UHV system show a small carbon peak and a lower calcium peak as can be seen in Figure 6.1a. The atomic concentrations determined from this set of AES results are shown in Table 6.1. Initially, carbon has an atomic concentration of $C_C = 0.11$, while $C_{Ca} = 0.07$. The oxygen peak indicating $C_O = 0.50$, and the iron peak indicating $C_{Fe} = 0.33$ are also clearly visible.

In order to remove the carbon from the surface, the sample was annealed for 15 hours at 950 ± 20 K. The Auger spectrum after this annealing stage (Figure 6.1b) shows a pronounced calcium peak (corresponding to $C_{Ca} = 0.10$), while the carbon peak is no longer discernible. This indicates that carbon desorbs much more readily from the polished surface than the rough side. With further annealing stages, first at 950 ± 20 K for 60 hours (Figure 6.1c) and then for a further 37 hours (Figure 6.1d) the level of the calcium at the surface continued to increase, rising to $C_{Ca} = 0.19$. This indicates that the calcium was diffusing from the bulk of the sample at these high temperatures. It should be borne in mind that the length of these annealing stages quoted here is in addition to the previous annealing stages that the sample underwent during the studies of the unpolished side.

It is worth noting that the initial surface atomic concentrations before annealing are in agreement with the values obtained for the unpolished face after its final anneal. It therefore appears that the annealing process is having the same effect on both the polished and unpolished sides of the sample. In addition, after the sample was exposed to air and re-introduced into UHV with the polished face exposed, the level of carbon on the sample surface remained quite low and comparable to the calcium level. The carbon present on the surface at this point is probably a combination of the residual carbon left after the annealing as well as carbon from air-borne hydrocarbons. It is also interesting to note that the level of carbon contamination was much greater ($C_C = 0.94$) when the sample was initially cleaned in ethanol and introduced into the vacuum system with its unpolished side exposed.

As in the case of the unpolished side of this sample, the annealing tem-

Table 6.1: Surface Atomic Concentrations of Polished Magnetite

<i>Anneal time (hours)</i>	<i>Anneal temp. (K)</i>	C_C	C_{Ca}	C_O	C_{Fe}
0	–	0.11	0.07	0.50	0.33
15	950 ± 20 K	0.00	0.10	0.48	0.42
60	950 ± 20 K	0.00	0.13	0.45	0.41
37	950 ± 20 K	0.00	0.19	0.43	0.38

perature of 950 ± 20 K leads to the diffusion of contaminants from the bulk, although no trace of sulphur was observed. Therefore, in order to obtain a clean magnetite surface, it appears that a lower anneal temperature (possibly of 900 ± 20 K) should be used for a longer period of time.

6.2 LEED patterns

The LEED pattern of the polished side was much sharper than that seen on the unpolished side of the sample. Before annealing, distinct diffraction beams consistent with a (1×1) termination of the surface can be seen, but these are very faint, and possibly reflect the bulk structure of the sample. After annealing the sample for 15 hours at 950 ± 20 K the LEED images showed bright well-defined spots, as shown in Figure 6.2a. The inset shows a computer generated pattern with the same symmetry. From these images a surface unit cell with primitive vector length of about 7 ± 1 Å can be calculated using a technique which is described in detail elsewhere [25]. This

is consistent with the size of an unreconstructed primitive surface unit cell which would have a primitive vector length of 6 \AA , and suggests that the unstable polar surface of magnetite has been stabilized by the presence of contaminants. However, due to experimental constraints related to the LEED equipment used in this study, the accuracy of the numerical values obtained from the LEED patterns is limited and they should be treated with caution.

As Figure 6.2b shows, subsequent annealing for 60 hours at this temperature led to the appearance of satellite spots. These additional diffracted beams indicate the presence of a reconstructed sample surface, possibly consisting of orthogonal domains of a $p(1 \times 4)$ structure. Linear features which have been referred to as nanoterraces in other studies [24–26] appear in the corresponding STM images and will be discussed in greater detail below. An additional 37 hours of annealing at $950 \pm 20 \text{ K}$ caused the LEED pattern to become fainter, indicating that the surface structure had become more disordered after this annealing stage. It is possible that this poor surface structure results from an overlayer formed by the high calcium atomic concentration of $C_{Ca} = 0.19$ at the surface after the final annealing stage.

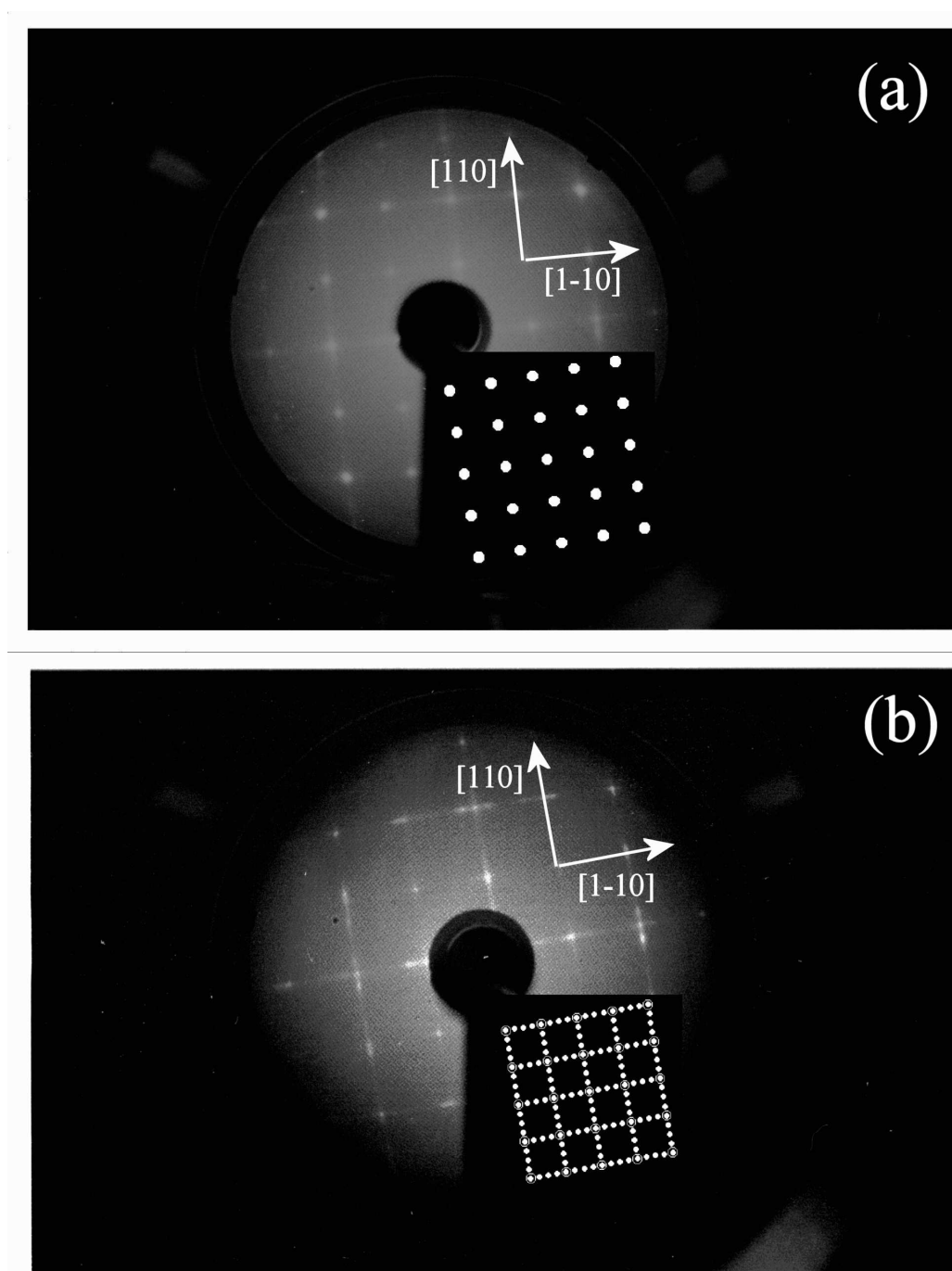


Figure 6.2: LEED patterns recorded on the polished Fe_3O_4 (001) surface. (a) After a 15 hour anneal at 950 ± 20 K a (1×1) pattern is observed, indicating a stabilized bulk termination of the surface. $E_{beam} = 93$ eV. (b) Satellite spots indicating a $p(1 \times 4)$ reconstructed surface appear after a subsequent 60 hour anneal at 950 ± 20 K. $E_{beam} = 82$ eV.

6.3 STM images

As expected, the height variation on the polished side of the sample was much less than on the unpolished side and high resolution STM images could be obtained routinely. After the sample had been re-loaded into the UHV system, but before it had been annealed again, the surface of the sample shows the square terraces that are expected from the cubic structure of magnetite, and are shown in Figure 6.3a. A smaller area scan (Figure 6.3b) shows that the surface is covered in clusters. These clusters are similar to those seen on the unpolished side of the sample and are probably composed of carbon or calcium (possibly in the form of CaO or $CaFe_2O_4$) as the corresponding AES spectrum shows $C_C = 0.11$ and $C_{Ca} = 0.07$.

Unusually, long terraces arranged in the form of steps can also be seen on the sample, as shown in Figure 6.3c and Figure 6.3d. These steps are similar to those seen on vicinal surfaces such as $Mo(110)$. Some curvature of the steps can be seen in the lower part of these images. This is attributed to the drift of the piezo tube scanner which occurs after it is moved to a new scan area. The height difference between adjacent large terraces was measured using a histogram of the locally plane fitted surface, and was found to be around 15 ± 2 Å. This corresponds to the height of two bulk unit cells which measure 8.4 Å each in magnetite. There appear to be several poorly resolved narrow terraces in between the larger terraces. However, due to the presence of the clusters on the surface it is difficult to accurately determine their height. The miscut from the (001) plane due to the variation in the sample polishing has possibly led to these long terraces and regular steps.

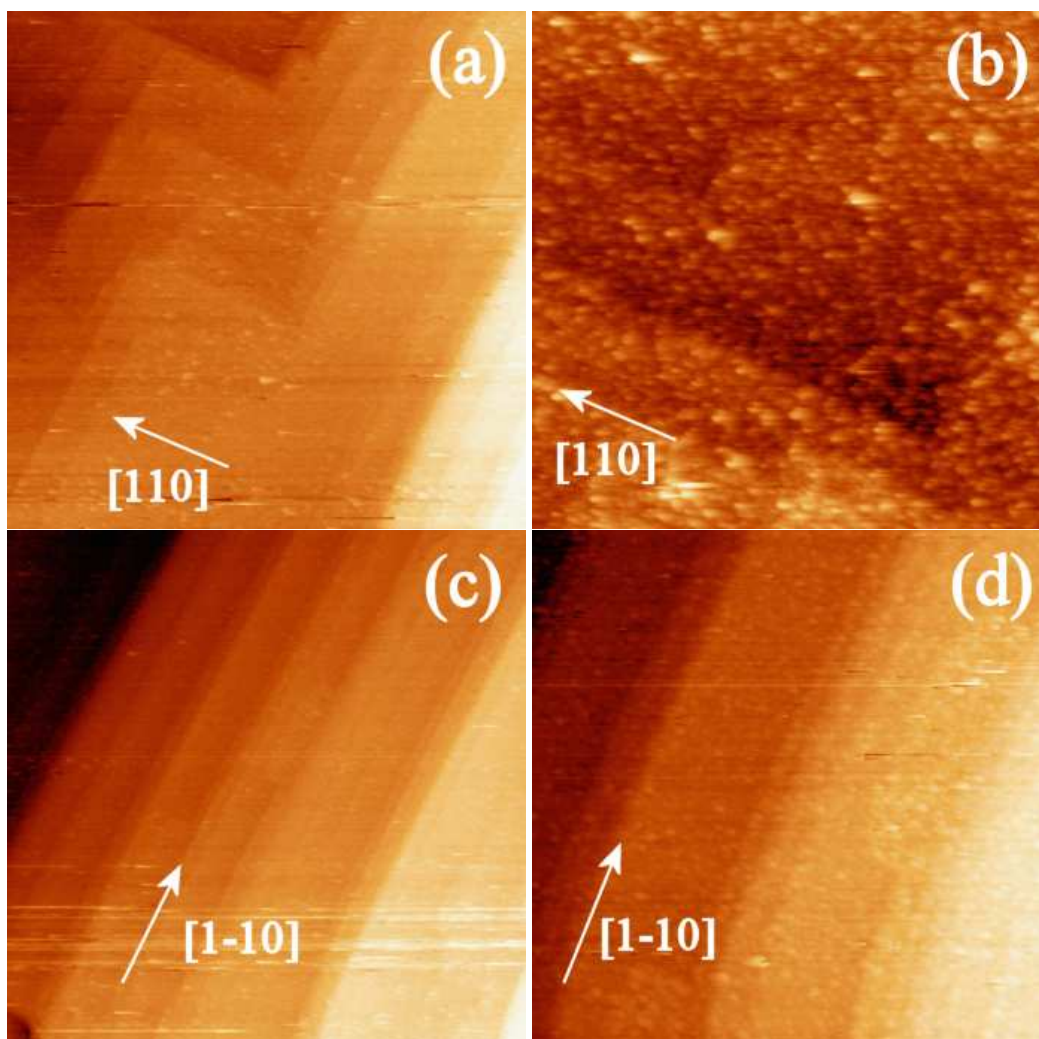


Figure 6.3: Images of the Fe_3O_4 (001) polished surface after it was re-introduced into the UHV chamber and after being annealed face down during experiments on the rough side of the sample. (a) This $500nm \times 500nm$ scan shows square terraces. (b) Clusters can be seen on the surface in this $100nm \times 100nm$ scan. (c) A $500nm \times 500nm$ scan showing the unusual long terraces that are similar to those on a vicinal surface. (d) The long terraces can be seen in more detail in this $200nm \times 200nm$ scan. All images were scanned with $V_{bias} = 1$ V, $I_t = 0.1$ nA and Tip = W.

6.3.1 15 Hour Anneal

After an anneal time of 15 hours at 950 ± 20 K, the STM images of the surface show irregular terraces, with apparently curved edges, as can be seen in Figure 6.4a. Analysis of the corresponding AES spectrum indicates that $C_{Ca} = 0.10$, and that no carbon is present.

The irregular structure of the terrace surface itself can also be seen in a closer view in Figure 6.4b. The surface of the terraces appear to have dendritic channels in them. These holes have a mean depth of 1.9 ± 0.2 Å. The spacing between equivalent planes in the bulk magnetite unit cell is 2.1 Å. The similarity between this and the depth of the holes indicates that the two levels imaged correspond to equivalent planes of the unit cell. This interpretation assumes that no significant relaxation of the interlayer spacing has taken place at the surface. However, significant relaxation of the spacing between the layers nearest the surface has been observed by other studies [73, 74].

Periodically spaced lines which appear to be composed of rows of single atoms can be seen in Figure 6.4c. These rows are clearer when the image is processed by differentiating the measured z values with respect to the x -axis, and the resulting image is shown in Figure 6.4d. Some of the rows appear to be grouped together and this might indicate the onset of nanoterraces. The periodicity of these rows, measured by a line profile perpendicular to their direction, is 6.6 ± 0.7 Å. This is consistent with the distance of 5.9 Å between adjacent rows of iron ions in octahedral positions in the bulk unit cell. These images were scanned with a W tip, and it is interesting to note that no regular corrugation along these atomic rows was observed. Such corrugation

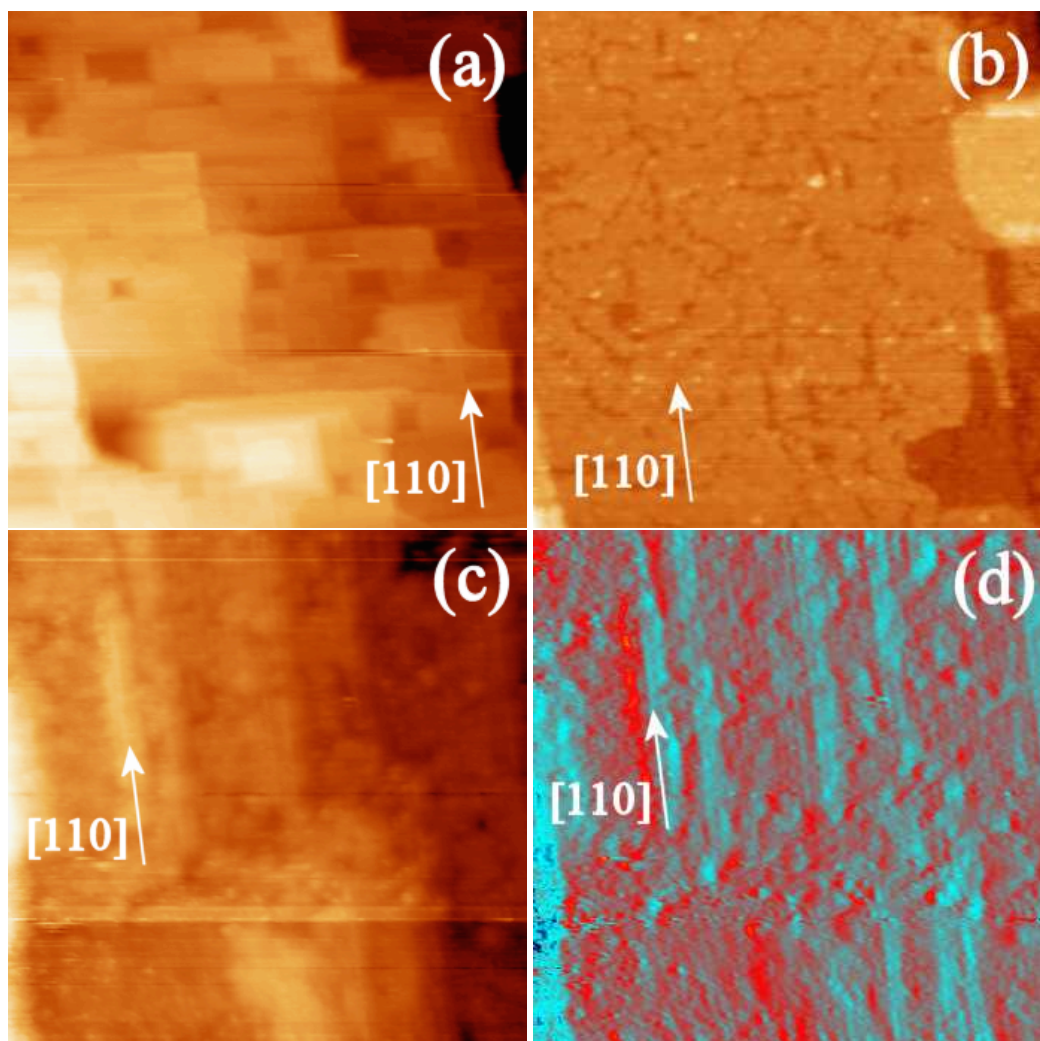


Figure 6.4: These images were scanned on the Fe_3O_4 (001) polished surface after a 15 hour anneal at 950 ± 20 K. (a) Irregular terraces can be seen in this $500nm \times 500nm$ scan. (b) This $80nm \times 80nm$ scan shows the dendritic channels in the terraces. (c) This high resolution $30nm \times 30nm$ scan shows the presence of what are apparently atomic rows. (d) This processed version of the image shown in (c) enables the atomic rows to be seen more clearly. All images were scanned with $V_{bias} = 1V$, $I_t = 0.1nA$ and Tip = W.

has been imaged in other studies with magnetic tips and is apparently due to charge ordering on the surface [26, 75].

The rows at the bottom left of this image appear to run at an angle to those in the rest of the image. Rows on the same scan lines at the right of the image do not show this variation in orientation indicating that this change in angle is not due to tube scanner drift. The orientation of these rows at a small angle to those on adjacent terraces indicates that a different reconstruction may be present in that area of the sample, or that the rows have formed at slightly different orientations.

In order to gain an overview of the surface topography, the data from one of the STM images acquired during this experimental session has been plotted in a 3D representation, shown in Figure 6.5. This image clearly shows the “right-angle” structure and terraces of the magnetite (001) surface.

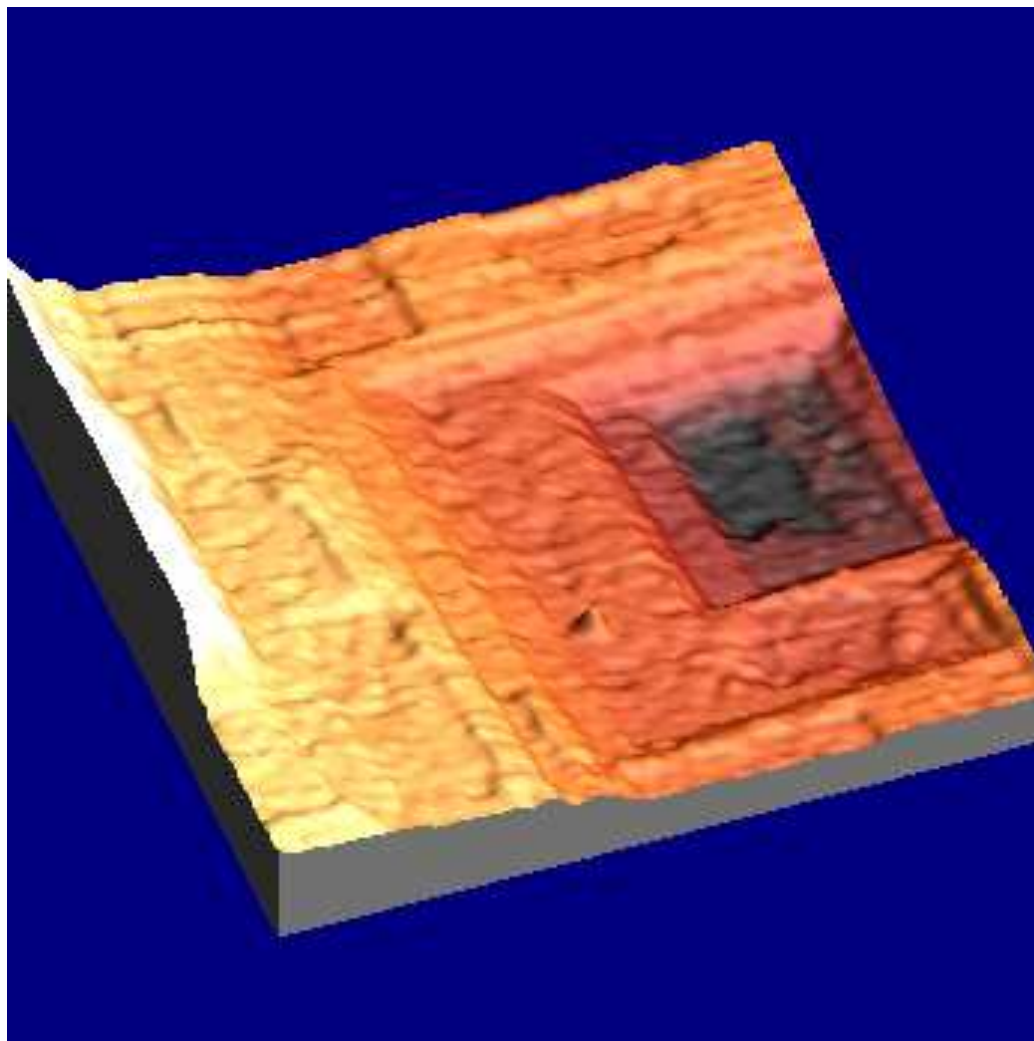


Figure 6.5: A 3D representation of a $100nm \times 100nm$ scan taken on the polished face of the magnetite sample after a 4 hour anneal. The terraces on the surface can be seen clearly. $V_{bias} = 1V, I_t = 0.1nA, Tip = W$.

6.3.2 60 Hour Anneal

A 60 hour anneal at a temperature of 950 ± 20 K led to the appearance of linear features on the surface, as shown in Figure 6.6. These rows are regularly spaced and are similar to the 1D reconstructions or “nanoterraces” observed in other studies [24, 26, 27, 76, 77]. Large area scans such as that shown in Figure 6.6a show that the rows are present on all the terraces imaged, and that the rows generally run in mutually perpendicular directions on adjacent terraces. However, rows in different parts of the same terrace also run perpendicular to one another occasionally, as can be seen in Figure 6.6b. This indicates that the rows start or nucleate at different points leading to slightly different orientations.

The periodicity of the nanoterraces in Figure 6.6b which run in the $[110]$ direction in the image is 37 ± 4 Å. The small number of nanoterraces which run in the $[1\bar{1}0]$ direction on the right hand side of this image have a similar periodicity of 29 ± 3 Å. The topography of the nanoterraces themselves can be seen more clearly in Figure 6.6c. Faint rows can be seen in the nanoterraces as well as a region where three nanoterraces merge into two. These apparently atomic rows are also visible in Figure 6.6d, which is a smaller area scan of the region in which the nanoterraces merge in Figure 6.6c. It appears that the nanoterraces are either 4 or 5 atomic rows wide which can be linked to the $p(1 \times 4)$ structure of the LEED patterns. The LEED patterns are also streaked in nature, reflecting the stepped structure of the surface with many terraces present. These rows have a periodicity of 5.4 ± 0.5 Å which is consistent with the spacing between rows of octahedral iron ions. The nanoterraces are oriented along the same $[110]$ crystallographic direction as the octahedral Fe

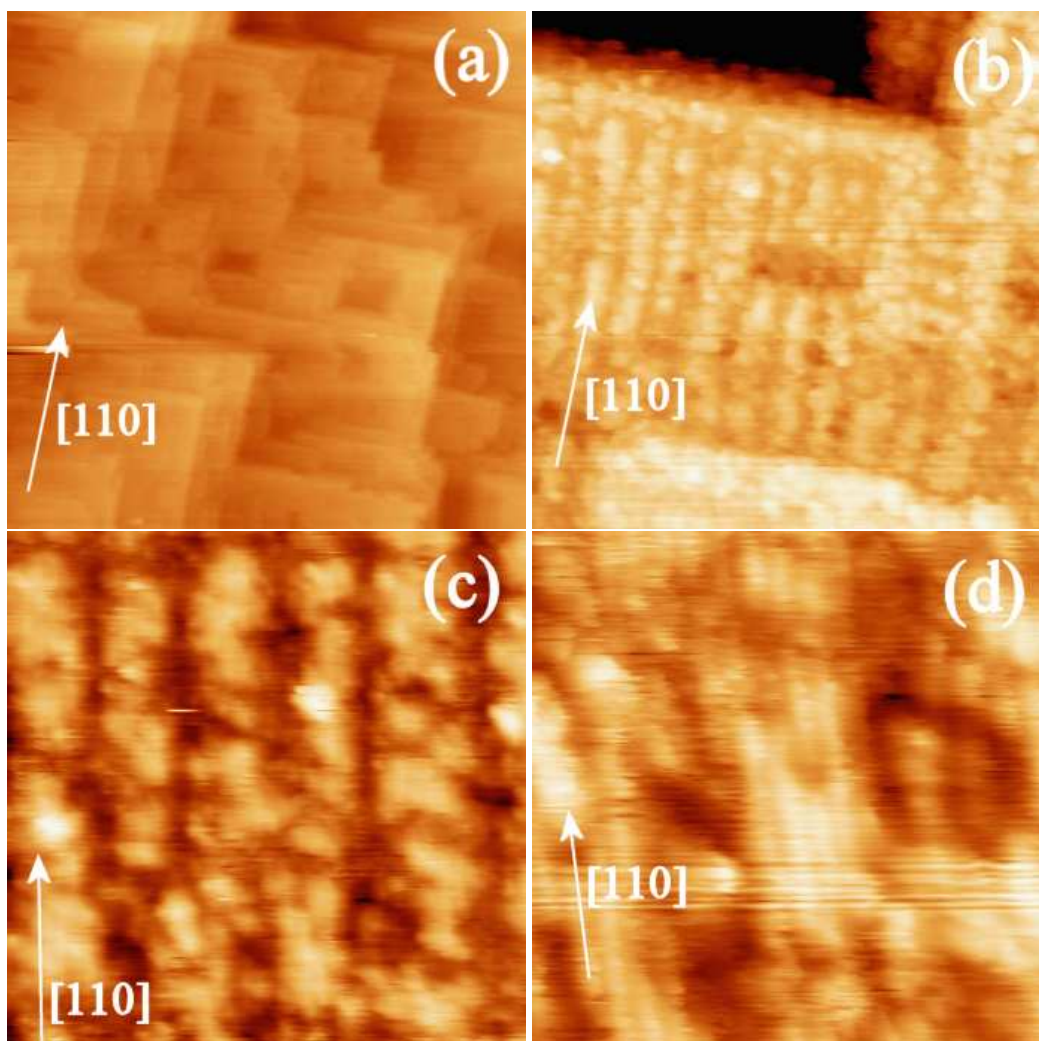


Figure 6.6: STM Images of the Fe_3O_4 (001) polished surface after another 60 hour anneal at 950 ± 20 K. (a) This large area $500nm \times 500nm$ scan shows the presence of nanoterraces on the surface. (b) The perpendicular nature of the angle between some of the rows on the same terrace is shown in this $50nm \times 50nm$ scan. (c) This $20nm \times 20nm$ small area scan shows the topography of the nanoterraces themselves. (d) Rows, apparently atomic in nature, can be seen in this $10nm \times 10nm$ image. All images were scanned with $V_{bias} = 1.5$ V, $I_t = 0.1$ nA and Tip = W.

sites. The nanoterraces are quite linear, as can be seen in Figure 6.7 which is a 3D representation of the data shown in Figure 6.6b.

6.3.3 37 Hour Anneal

Further annealing to 950 ± 20 K for 37 hours led to further changes in the sample surface. The STM tip during this session was unstable, and two tip changes can be seen in Figure 6.8a. The large number of clusters on the surface can be seen in Figure 6.8b. In order to improve the image quality voltage pulses were applied to the tip. These tip pulses were programmed by the author using the “nanostructuring macro language” feature of the Omicron SPM software, and consisted of a 10 V pulse applied for 50 ms. This is similar to the pulses that were applied using the Tops controller in the past. The tip consistently recovered after each voltage pulse, and a cluster of material could be seen at each point on the sample where a pulse had been applied. This indicates that material was picked up by the tip during scanning which reduced its imaging resolution. The voltage pulse applied then jettisoned this material from the tip onto the sample which enabled it to scan once again.

The clusters on the sample surface were probably partly composed of calcium (possibly in the form of CaO or $CaFe_2O_4$) and did not contain elemental carbon, as calcium was the only element other than iron and oxygen present in the corresponding AES spectrum. This indicates that this anneal stage has led to the segregation of a significant amount of calcium from the bulk of the crystal, and that this calcium has diffused to the surface where it has formed an overlayer containing clusters which reduce the image quality.

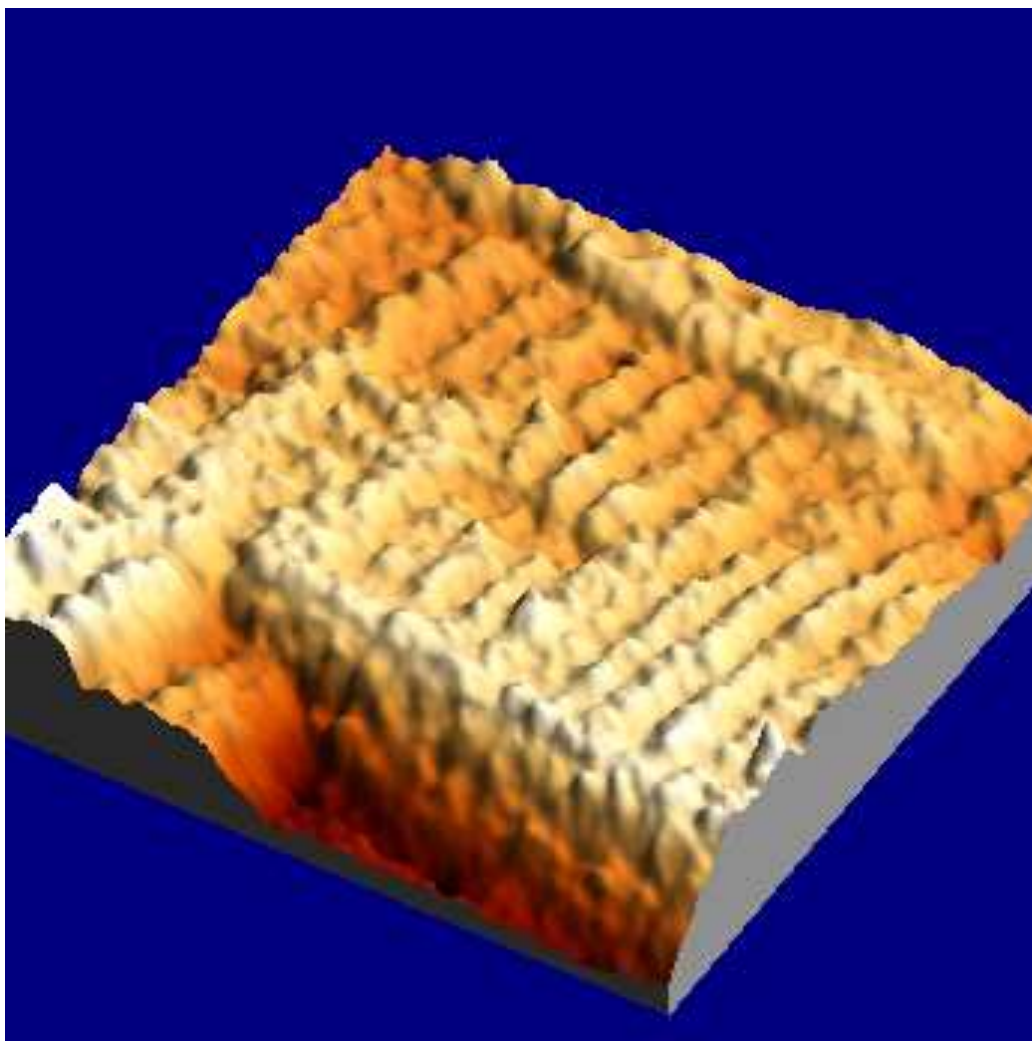


Figure 6.7: A rotated 3D representation of a $50nm \times 50nm$ STM image shown in Figure 6.6b. This image was taken taken on the polished face of the magnetite sample after a 60 hour anneal. The linear nature of the nanoterraces is evident. $V_{bias} = 1.5$ V, $I_t = 0.1$ nA and Tip = W.

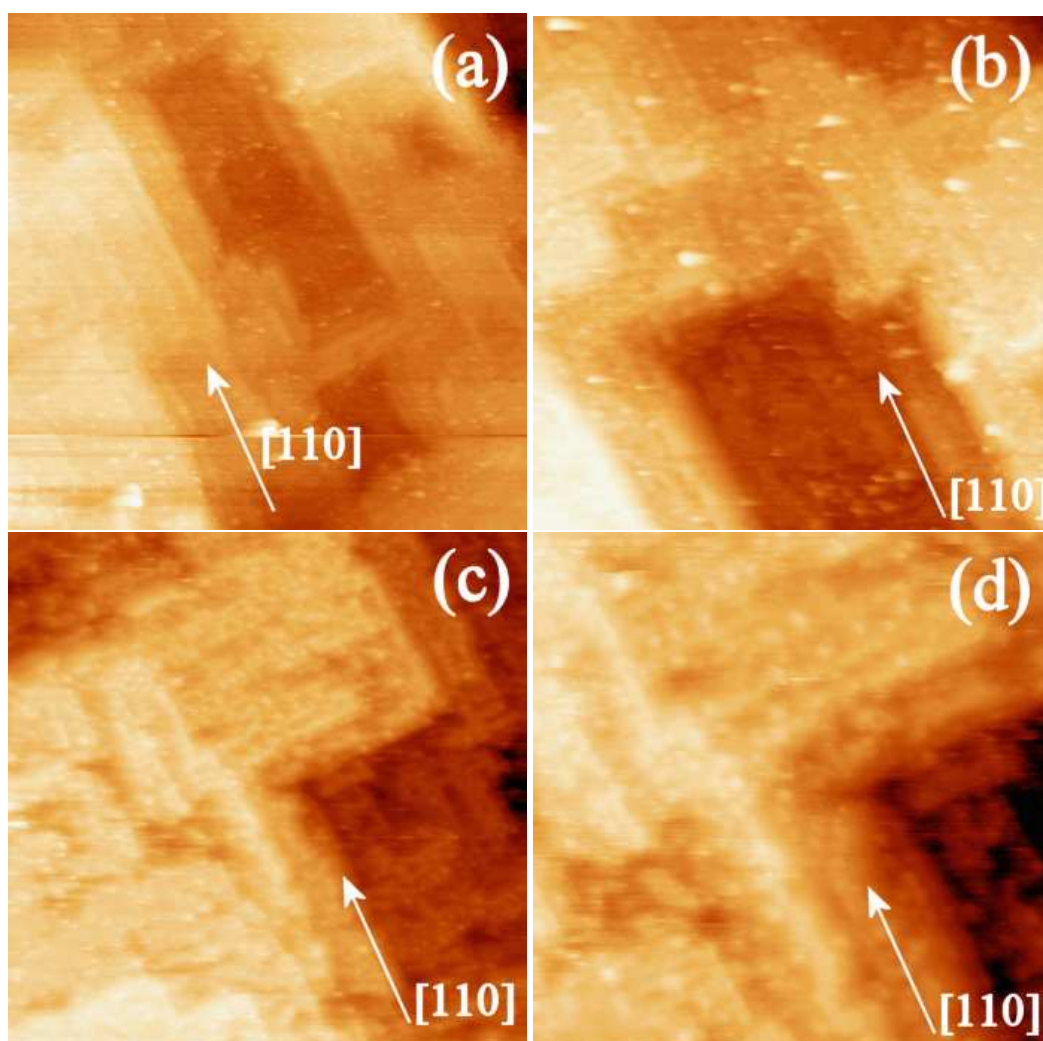


Figure 6.8: These STM images were scanned on the polished magnetite surface after the final 37 hour anneal at 950 ± 20 K. (a) The image quality was unstable during this scanning session, probably due to the presence of a significant amount of calcium on the surface. Two tip changes can be seen in this $200nm \times 200nm$ image. $V_{bias} = 1.5$ V, $I_t = 0.1$ nA. (b) A large number of clusters on the surface can be seen in this $100nm \times 100nm$ scan. $V_{bias} = 1.5$ V, $I_t = 0.1$ nA. (c) Features similar to nanoterraces can be seen in this $100nm \times 100nm$ sized image. $V_{bias} = 1$ V, $I_t = 0.1$ nA. (d) A smaller $50nm \times 50nm$ scan enables the periodicities of the rows to be measured using line profiles. $V_{bias} = 1$ V, $I_t = 0.1$ nA. All images were scanned with a W tip.

During periods where the tip quality was consistent, several features similar to nanoterraces were observed. On relatively large area scans such as Figure 6.8c, these features had a periodicity of about 28 ± 3 Å. The periodicities measured in a smaller area scan (Figure 6.8d) depend on the orientation of the linear features. Line profile measurements indicate that the rows in the $[1\bar{1}0]$ direction repeat every 31 ± 3 Å. Line profiles on the rows in the $[110]$ direction, however, give a value for the periodicity of 14 ± 1 Å. This variation is unlikely to be due to drift in the tube scanner as the two sets of rows are perpendicular to one another as expected, and any drift present would have distorted the angle between the rows. It is therefore probable that the variation in the periodicity indicate a change in the structure of the array of nanoterraces on some terraces induced by the calcium overlayer.

6.4 Overview

Taken together, the results presented in this section indicate that calcium diffusing from the bulk of the sample has a significant influence on the surface structure of $Fe_3O_4(001)$. Similar effects have been seen in thin films of magnetite grown on MgO substrates [27], and although that study attributed the reconstructions to the presence of Mg, it is known that Ca often segregates to the MgO surface and it is possible that the surface structure was caused by Ca [78, 79]. The sequential anneal stages applied to the magnetite sample studied here leads to the segregation of the calcium within the bulk of the sample and it then diffuses to the sample surface. The presence of calcium causes linear reconstructions in the shape of nanoterraces 4 or 5 atomic rows wide to form. The variation in the width and periodicity of the nanoterraces

indicates that the surface is not fully reconstructed. As indicated by AES, the surface of the magnetite sample studied here is non-stoichiometric and varies as a function of anneal time. It is likely that similar samples that were studied previously also contained impurities such as calcium, but that this was not detected by the AES equipment used then. The formula unit of the ferrite compound formed by the combination of Ca and Fe_3O_4 at the surface is likely to be of the form of $Ca_xFe_{3-x}O_4$ [26].

It is interesting to note that the $(\sqrt{2} \times \sqrt{2})R45^\circ$ reconstruction often seen on clean magnetite (001) surfaces was not seen here. Instead, either a (1×1) or a $p(1 \times 4)$ diffraction were observed by LEED, consistent with the presence of impurities at the surface. The presence of the $(\sqrt{2} \times \sqrt{2})R45^\circ$ could in future be used as an effective and efficient technique to gauge the purity of a given magnetite sample surface and avoid the time consuming use of AES and STM techniques.

These nanoterraces could provide useful templates for patterned magnetic media as their dimensions are well below those achievable with conventional lithographic techniques. By depositing a thin film of iron on the nanoterraces a well-ordered system with unique magnetic properties could be developed. The presence of calcium should also have an interesting effect on the electrical and magnetic properties of magnetite, including its Verwey transition temperature which is particularly relevant for investigations of magnetite at low temperatures.

Chapter 7

Conclusions

The experiments carried out in this study have investigated a number of interesting features of nanomagnetic systems. In the case of the iron films on molybdenum, several films of different thicknesses were grown. During the preparation of the substrate an irregular vicinal Mo(110) surface was observed. The step edges of the surface were rough and the terraces were not uniform or defined by straight edges. Subsequent preparation processes improved the surface quality.

The AES results on a film of 1.2 ML of iron grown on Mo(110) showed the presence of oxygen, indicating that an iron oxide may have formed on the sample surface. The corresponding LEED pattern indicated a $p(2 \times 2)$ reconstruction of the surface. The STM scans on this film showed the expected mixture of the step-flow and the island nucleation growth modes. The resulting film does not appear to have an almost completely closed first layer as was seen in the case of a similar film grown in another study [48]. This variation is probably due to the different deposition rates used.

In a subsequent experiment, a much thicker iron film of 3.6 ML was

grown. This resulted in very large islands with a width and length of approximately 200 nm. In the area between the islands, STM scans with an antiferromagnetic MnNi tip show the presence of wide terraces of varying surface roughness. These terraces are possibly caused by the overlap of iron layers producing a transition from one monolayer thick stripe to a two monolayer thick stripe. It is possible that the contrast observed between these nanowires is caused by the magnetic sensitivity of the MnNi tip. Further experiments with an external magnetic field applied to the sample during the STM experiments should help to confirm whether this is the case. It is also possible that the different roughness is due to variations in the crystal structure as a function of film thickness.

The extensive experiments carried out on the polished and unpolished surfaces of a magnetite crystal provided interesting results that help interpret previous studies. The use of sensitive AES equipment has meant that the chemical composition of the crystal surface can now be studied in greater detail. Previous work by researchers in this group on magnetite did not have access to this equipment, and a more complete analysis of those results can now be carried out [24,25].

7.0.1 Unpolished Magnetite Surface

The unpolished face of the magnetite surface was studied first. It is interesting to note that although the sample studied here was grown artificially using the skull melting technique by the group of Professor Honig in Purdue University, USA, it still contained a large amount of impurities. Other similar artificial crystals have also been found to contain contaminants [26]. Initially, the

atomic concentration of carbon at the sample surface was determined to be approximately $C_C = 0.94$ by AES. In order to clean the sample surface, the crystal was annealed for a number of hours first at a temperature of 900 ± 20 K and then at 950 ± 20 K. During these annealing stages, the amount of carbon at the surface decreased, and during one session a small amount of sulphur which had apparently diffused from the bulk was also observed. A significant amount of calcium also diffused from the bulk of the crystal during the annealing procedure and after the final anneal stage the atomic concentration of carbon was $C_C = 0.10$ while that of calcium was $C_{Ca} = 0.07$. Although the higher anneal temperature of 950 ± 20 K resulted in the desorption of carbon from the surface, it also apparently caused the segregation of impurities such as calcium from the bulk. It would therefore be appropriate in future studies to anneal at a lower temperature of approximately 900 ± 20 K in order to obtain a magnetite surface with less impurities.

The LEED pattern on the unpolished side of the sample was very faint indicating that the surface was quite disordered. The presence of a faint (1×1) pattern suggests that the normally polar and unstable Fe_3O_4 (001) surface had been stabilized by the contaminants present at the surface. STM images confirmed the disorder and roughness of this side of the sample. Initially, long depressions were present on the surface. Annealing caused the sample surface topography to change and it is probable that large mass transport effects occurred effectively regrowing the Fe_3O_4 surface.

After the final annealing stage, faint rows with a separation of 7 ± 1 Å were observed by STM. As this distance corresponds to the spacing between rows

of octahedral Fe ions, it appears that these are either the Fe ions themselves or contaminants that have formed a reconstruction which reflects the periodicity of the inverse spinel crystal structure.

It appears that a combination of large movements of material at the sample surface and the desorption of a carbon overlayer cause the topography of the unpolished sample face to change and become smoother. However, large topography variations remained present at the sample surface, making it unsuitable for STM scans.

7.0.2 Polished Magnetite Surface

The polished side of the artificial magnetite crystal was more suitable for STM experiments as it did not contain major height variations. Even though the sample was exposed to air for a short period of time while it was being prepared, the carbon concentration as determined by AES was $C_C = 0.11$. This is significantly lower than that seen for the initial scan of the rough side of the sample which had been cleaned in ethanol. This indicates that the primary source of carbon on the surface might be the ethanol used to clean the crystal and not airborne hydrocarbons, although rough surfaces would be expected to have more carbon present in general. Carbon also desorbed from the polished side of the sample at a faster rate than on the rough side, and after a 15 hour long anneal at 950 ± 20 K no carbon was detected. However, a large amount of calcium did diffuse from the bulk of the crystal during the annealing stages, and the calcium concentration eventually rose to $C_{Ca} = 0.19$. This again suggests that a lower annealing temperature would be appropriate in order to prepare an uncontaminated magnetite surface.

The LEED patterns on the polished side of the sample were quite sharp. They initially indicated a (1×1) termination of the surface, and a surface unit cell with a primitive vector length of $7 \pm 1 \text{ \AA}$. This (1×1) termination is consistent with the presence of stabilizing contaminants, as seen in the AES analysis of the sample. Further annealing led to the appearance of satellite spots in the LEED pattern. This corresponds to orthogonal domains of a $p(1 \times 4)$ reconstruction, which appear as nanoterraces in the corresponding STM images. During the final annealing stage, the LEED pattern became fainter and it is possible that the poor surface structure indicated by this is caused by a calcium overlayer at the surface.

Large area STM scans of the sample before it was annealed with the polished side exposed show the square terraces expected with cubic crystals such as magnetite. However, a closer inspection of the surface with STM reveals the presence of clusters on the surface. These clusters are similar to those seen on the unpolished side of the sample, and probably consist partly of C and Ca, possibly in the form of CaO or $CaFe_2O_4$, as suggested by an analysis of the AES spectra.

Unusually, long terraces separated by narrow steps, similar to those seen on the surface of vicinal crystals such as the Mo(110) sample studied here were also observed. This surface structure was possibly caused by the slight misalignment of the polishing plane in the region being scanned. It is interesting to note that the regularity of this surface structure, and the presence of long terraces, make it an interesting candidate for further magnetic experiments (possibly involving the deposition of iron films). Such a sample could be compared to other widely studied stepped surfaces, and possibly lead to

the development of new magnetic device applications for “miscut” magnetite crystals.

Irregular terraces, apparently with curved edges, were observed after annealing the sample. The terrace surfaces themselves were uneven, and contained dendritic channels in them. The depth of these channels was 1.9 ± 0.2 Å which is consistent with the STM imaging equivalent planes of the magnetite bulk unit cell which are separated by 2.1 Å, and also consistent with the 14% relaxation of the first interlayer spacing that was determined by other studies [73]. Periodically spaced atomic rows, apparently consisting of octahedral iron ions were also observed. It is interesting to note that the STM images of these rows taken with a W tip show no periodic corrugation along the rows. Such a corrugation has been noted on clean magnetite during STM sessions with a MnNi tip [26] and attributed to charge ordering at the surface. It is possible that this discrepancy is due to the absence of spin sensitivity in the W tip, although the different stoichiometry of the surfaces studied should also be taken into consideration.

Further annealing stages led to the formation of linear features apparently several atomic rows wide and consistent with the $p(1 \times 4)$ reconstruction observed in the corresponding LEED pattern. These one-dimensional reconstructions are similar to those seen in previous studies [24, 25, 77]. In the $[110]$ direction the periodicity of the nanoterraces was 37 ± 4 Å. Their average periodicity in the $[1\bar{1}0]$ direction was 29 ± 3 Å. In some images, the orientation of the rows varies slightly, while in others rows running perpendicular to one another meet on the same terrace. This indicates that these narrow terraces may have formed at separate locations and grown with dif-

fering orientations. Atomic rows were resolved in the nanoterraces indicating that they were approximately four or five atomic rows wide. The distance between each row of $5.4 \pm 0.5 \text{ \AA}$ and their orientation along the $\langle 110 \rangle$ crystallographic directions is consistent with octahedral iron sites being imaged. These nanoterraces form in a manner similar to self-directed growth in other systems [80], and spontaneous pattern formation by self-assembly has been investigated in several magnetic [81] and semiconductor [82,83] systems. These rows could provide useful templates for the formation of regular magnetic structures by the subsequent deposition of a magnetic material such as iron.

The final anneal stage led to the concentration of calcium at the surface rising to $C_{Ca} = 0.19$, and STM scans during this session were unstable. However a short voltage pulse applied to the tip consistently improved image quality, implying that material was picked up by the tip as it scanned across the sample surface, thereby reducing its imaging resolution. The applied voltage pulse then caused this material to be jettisoned from the tip and the image quality improved. The clusters observed on the contaminated sample surface probably consisted largely of calcium, possibly in the form of CaO or $CaFe_2O_4$. Several high resolution images of this surface were obtained, and nanoterraces were observed on the larger terraces. Unlike the previous nanoterraces observed, the distance between them varied depending on their orientation. Nanoterraces in the $[1\bar{1}0]$ direction had a periodicity of $31 \pm 3 \text{ \AA}$, while those in the $[110]$ direction repeated every $14 \pm 1 \text{ \AA}$.

From these results it is evident that a significant amount of calcium is present in the artificial magnetite crystal studied here, and that the presence

of this calcium at the surface strongly influences the morphology of the surface. Although it was previously thought in the absence of a sensitive AES analysis that other crystals from this batch of artificial magnetite were pure this is now unlikely to be the case [24, 25]. Reconstructions similar to the linear features observed here are unlikely to have formed on a clean surface and are more likely to be induced by a contaminant, probably Ca (although K and S are also possible) in a manner similar to the reconstructions attributed to the presence of Mg observed in other studies [27]. However, it is known that Ca often segregates to the MgO surface [78, 79], and it is possible that Ca and not Mg caused the 1D reconstructions observed in Reference [27]. The coloured films previously attributed to an iron diffusion effect may have been related to the diffusion of contaminants from the bulk of the crystal being studied [25]. Other research has shown that the optical properties of magnetite crystals are also strongly influenced by the technique used to polish them [43].

It is possible that the calcium diffusing from the bulk replaces some of the iron ions in the surface layer. The resulting chemical structure of the compound at the surface may then be written as $Ca_xFe_{3-x}O_4$, where x represents the fraction of the iron ions replaced by the calcium. This diffusion and segregation from the bulk of the crystal could be driven by size or charge balancing properties, in a manner similar to those apparently leading to the segregation of Mg through thin magnetite films [27]. It is also possible that a non-stoichiometric interface is formed with a gradually decreasing calcium concentration with depth in a manner similar to that observed during the interaction of potassium with $Fe_3O_4(111)$ [84]. The orientation of the linear

terraces along the $\langle 110 \rangle$ directions suggests that the rate of segregation of calcium is dependent on the crystallographic direction, as suggested in Reference [27].

As no $(r\sqrt{2} \times r\sqrt{2})R45^\circ$ reconstruction [74,85] was observed either by LEED or STM during this set of experiments on polished or unpolished magnetite, it is likely that this reconstruction only forms on stoichiometric magnetite surfaces. Therefore, the analysis of the LEED pattern on a sample could provide an effective and efficient method of determining the standard of surface cleanliness during sample preparation.

7.1 Further Work

It is clear from these results and from other studies [84] that magnetite displays a fascinating variety of surface structures depending on the stoichiometry of the surface. It would be interesting in future studies to dope the magnetite surface with a variety of impurities, including Mg and Ca, in different concentrations and to observe the resulting topography. Although impurities are expected in natural magnetite crystals and calcium is one of the most common impurities in metal oxides [79], the preparation of a stoichiometric surface would be more suitable for SP STM experiments. Such stoichiometric surfaces can be prepared by ion sputtering, or by depositing thin films on non-magnetic substrates by Molecular Beam Epitaxy (MBE) [86,87]. In addition, the significant effect of the calcium seen in this study sheds light on the importance of sample stoichiometry in other related fields. For example, in a powdered sample of magnetic material, there are many interfaces between the surfaces of different grains, and the properties of these interfaces could be

influenced by impurities. The presence of impurities should also have interesting effects on the magnetoelectronic properties of heterojunctions grown between different spinels.

Atomic resolution STM images at various temperatures and in applied magnetic fields with antiferromagnetic tips on other nanomagnetic systems could provide valuable extra information for an enhanced analysis of the data presented in this and other studies. The magnetite surface, either clean or with surface structures induced by impurity doping could provide useful substrates for the deposition of iron and other magnetic elements and compounds in technical applications. It would also be interesting to examine the (111) face of magnetite bulk crystals in the light of the understanding now developed of the (001) face.

It is hoped that the experiments carried out in this project have led to useful insights into the fundamental physical properties of technologically relevant nanomagnetic systems.

Bibliography

- [1] Carol E. Diebel, Roger Proksch, Colin R. Green, Peter Neilson, and Michael M. Walker. *Nature*, 406:299–302, 2000.
- [2] Robert M. Hazen. *Scientific American*, pages 63–71, April 2001.
- [3] R. H. Kodama. *Journal of Magnetism and Magnetic Materials*, 200:359–372, 1999.
- [4] G. A. Farnan, M. P. McCurry, and D. G. Walmsley. *Physica C*, (341–348):2335–2336, 2000.
- [5] J. Carney. *Medieval Irish lyrics*. Dolmen P., 1967.
- [6] J. A. Simpson and E. S. C. Weiner. *The Oxford English Dictionary*. Clarendon P., Oxford, second edition, 1989.
- [7] F. J. Himpsel, J. E. Ortega, G. J. Mankey, and R. F. Willis. *Advances in Physics*, 47(4):511–597, 1998.
- [8] The art of the quantum leap. *The Economist*, December 6, 2001.
- [9] C. Vinegoni, M. Cazzanelli, A. Trivelli, G. Mariotto, J. Castro, J. G. Lunney, and J. Levy. *Surface and Coatings Technology*, 124:272–277, 2000.

- [10] G. J. Hughes, P. Ryan, P. Quinn, and A. A. Cafolla. *Vacuum*, 57:131–138, 2000.
- [11] E. Dudzik, C. Müller, I. T. McGovern, D. R. Lloyd, A. Patchett, D. R. T. Zahn, T. Johal, and R. McGrath. *Surface Science*, 344:1–10, 1995.
- [12] S. Chandola, M. Cavanagh, J. R. Power, and J. F. McGilp. *Thin Solid Films*, 313–314:565–567, 1998.
- [13] J. N. Chapman and M. R. Scheinfein. *Journal of Magnetism and Magnetic Materials*, 200:729–740, 1999.
- [14] T. Shinjo and W. Keune. *Journal of Magnetism and Magnetic Materials*, 200:598–615, 1999.
- [15] F Nolting, A Scholl, J Stohr, JW Seo, J Fompeyrine, H Siegart, JP Locquet, S Anders, J Luning, EE Fullertonm, MF Toney, MR Scheinfein, and HA Padmore. *Nature*, 405:767–769, 2000.
- [16] C. Durkan and I. V. Shvets. *Journal of Applied Physics*, 80(10):5659–5664, 1996.
- [17] C. Durkan, I. V. Shvets, and J. C. Lodder. *Applied Physics Letters*, 70(10):1323–1325, 1997.
- [18] B. A. F. Puygranier and P. Dawson. *Ultramicroscopy*, 85:235–248, 2000.
- [19] E. Dan Dahlberg and Roger Proksch. *Journal of Magnetism and Magnetic Materials*, 200:720–728, 1999.
- [20] O. Yu. Kolesnychenko, R. de Kort, and H. van Kempen. *Surface Science*, 490:573–578, 2001.

- [21] D. Bürgler G. Tarrach H.-J. Güntherodt I.V. Shvets, R. Wiesendanger. *Journal of Applied Physics*, 71(11):5489–5499, June 1992.
- [22] Bode M, M Dreyer, M Getzlaff, M Kleiber, A Wadas, and R Wiesendanger. *Journal of Physics: Condensed Matter*, 11:9387–9402, 1999.
- [23] U. Schwertmann R. M. Cornell. *The iron oxides: structure, properties, reactions, occurrence and uses*. VCH, Weinheim, Germany, 1996.
- [24] C. Seoighe, J. Naumann, and I. V. Shvets. *Surface Science*, 440:116–124, 1999.
- [25] Ciarán Seoighe. *Surface studies of magnetite (100)*. PhD thesis, Trinity College Dublin, Ireland, October 1999.
- [26] Guido Mariotto. *Surface reconstructions of $Fe_3O_4(001)$* . PhD thesis, Trinity College Dublin, Ireland, October 2001.
- [27] J. F. Anderson, M. Kuhn, U. Diebold, K. Shaw, P. Stoyanov, and D. Lind. *Physical Review B-Condensed Matter*, 56:9902–9909, 1997.
- [28] C. Julian Chen. *Introduction to Scanning Tunneling Microscopy*. Oxford Series in Optical and Imaging Sciences. Oxford University Press, New York, USA, 1993.
- [29] Dawn Bonnell. *Scanning probe microscopy and spectroscopy: theory, techniques, and applications*. Wiley-VCH, New York, USA, 2001.
- [30] G. S. Duesberg, W. J. Blau, H. J. Byrne, J. Muster, M. Burghard, and S. Roth. Experimental observation of individual single-wall nanotube species by raman microscopy.

- [31] Thomas W. Tomblor, Chongwu Zhou, Leo Alexseyev, Jing King, Hongjie Dai, Lei Liu, C. S. Jayanthi, Meijie Tang, and Shi-Yu Wu. *Nature*, 405:769–772, 2000.
- [32] F. J. Himpsel, K. N. Altmann, G. J. Mankey, J. E. Ortega, and D. Y. Petrovykh. *Journal of Magnetism and Magnetic Materials*, 200:456–469, 1999.
- [33] A. Gupta and J. Z. Sun. *Journal of Magnetism and Magnetic Materials*, 200:24–43, 1999.
- [34] A. Kubetzka, M. Bode, O. Pietzch, and R. Wiesendanger. *Physical Review Letters*, 88(5):057201–1–4, 2002.
- [35] M. Tikhov and E. Bauer. *Surface Science*, 232:73–91, 1990.
- [36] Ulrich Gradmann. *Handbook of Magnetic Materials*, volume 7, chapter 1. Elsevier Science Publishers B.V., 1993.
- [37] R. C. O’Handley. *Modern magnetic materials: principles and applications*. John Wiley & Sons, Inc., 2000.
- [38] R. Skomski and JMD Coey. *Permanent Magnetism*. Institute of Physics, 1999.
- [39] JMD Coey. *Iron in Soils and Clay Minerals (Eds. J.W. Stucki, B.A. Goodman and U. Schwertmann)*, chapter 14, pages 397–466. Riedel, Dordrecht, 1988.
- [40] J. M. Hönig. *Journal of Alloys and Compounds*, 229:24–39, 1995.

- [41] V. A. M. Brabers, F. Walz, and Kronmüller. *Physical Review B*, 58(21):14163–14166, 1998.
- [42] Jürgen Osing. *Studies towards spin sensitive scanning tunneling microscopy*. PhD thesis, Trinity College Dublin, Ireland, October 1998.
- [43] Eugen Libowitzky. *European Journal of Mineralogy*, 6:187–194, 1994.
- [44] R. Wiesendanger, I. V. Shvets, and J. M. D. Coey. *Journal of Vacuum Science and Technology B*, 12(3):2118–2121, 1994.
- [45] Aidan Quinn. *Development of an ultra-high vacuum scanning tunneling microscope*. PhD thesis, Trinity College Dublin, Ireland, July 1996.
- [46] J. Naumann, J. Osing, A. J. Quinn, and I. V. Shvets. *Surface Science*, 388:212–219, 1997.
- [47] Paul W. Palmberg-Gerald E. Riach Roland E. Weber Lawrence E. Davis, Noel C. Macdonald. *Handbook of Auger Electron Spectroscopy, A Reference Book of Standard Data for Identification and Interpretation of Auger Electron Spectroscopy Data*. Physical Electronics Industries Inc., Eden Prairie, Minnesota, USA, second edition, 1976.
- [48] Shane Murphy. *Surface studies of the Fe/Mo(110) and Fe/W(100) epitaxial systems*. PhD thesis, Trinity College Dublin, Ireland, October 2000.
- [49] H. W. M. Salemink, Inder P. Batra, H. Rohrer, E. Stoll, and E. Weibel. *Surface Science*, 181:139–144, 1987.

- [50] David Tománek, Steven G. Louie, H. Jonathon Mamin, David W. Abraham, Ruth Ellen Thomson, Eric Ganz, and John Clarke. *Physical Review B*, 35:7790–7793, 1987.
- [51] J. Osing and I. V. Shvets. *Surface Science*, 417:145–150, 1998.
- [52] S. Murphy, J. Osing, and I. V. Shvets. *Applied Surface Science*, 144–145:497–500, 1999.
- [53] S. Murphy, J. Osing, and I. V. Shvets. *Journal of Magnetism and Magnetic Materials*, 198-199:686–688, 1999.
- [54] Massimiliano Cavallini and Fabio Biscarini. *Review of Scientific Instruments*, 71(12):4457–4460, 2000.
- [55] O. Albrektsen, H. W. M. Salemink, K. A. Mørch, and A. R. Thölen. *Journal of Vacuum Science and Technology B*, 12(6):3187–3190, 1994.
- [56] E. Anguiano, A. I. Oliva, and M. Aguilar. *Review of Scientific Instruments*, 69(11):3867–3874, 1998.
- [57] E. Anguiano, A. I. Oliva, and M. Aguilar. *Review of Scientific Instruments*, 69(11):3875–3878, 1998.
- [58] A. Hammiche, Yu Wei, I. H. Wilson, and R. P. Webb. *Review of Scientific Instruments*, 62(12):3010–3021, 1991.
- [59] G. Mariotto, M. D’Angelo, J. Kresnin, and I. V. Shvets. *Applied Surface Science*, 144–145:530–533, 1999.
- [60] G. Mariotto, M. D’Angelo, and I. V. Shvets. *Review of Scientific Instruments*, 70(9):3651–3655, 1999.

- [61] Julian C. Chen. *Applied Physics Letters*, 60(1):132–134, 1992.
- [62] J. Tapson and J. R. Greene. *Review of Scientific Instruments*, 68(7):2797–2799, 1997.
- [63] H. J. Elmers, J. Hauschild, and U. Gradmann. *Journal of Magnetism and Magnetic Materials*, 198–199:222–224, 199.
- [64] J. Osing, S. Murphy, and I. V. Shvets. *Surface Science*, 454–456:280–283, 2000.
- [65] H. Bethge, D. Heuer, Ch. Jensen, K. Reshöft, and U. Köhler. *Surface Science*, 331–333:878–884, 1995.
- [66] J. Osing and I. V. Shvets. *Journal of Magnetism and Magnetic Materials*, 198–199:734–736, 1999.
- [67] J. Malzbender, M. Przybylski, J. Giergiel, and J. Kirschner. *Surface Science*, 414:187–196, 1998.
- [68] J. Osing and I. V. Shvets. *Surface Science*, 433–435:440–444, 1999.
- [69] J. Hauschild, U. Gradmann, and H. J. Elmers. *Applied Physics Letters*, 72(24):3211–3213, 1998.
- [70] H. J. Elmers, J. Hauschild, and Gradmann. *Journal of Magnetism and Magnetic Materials*, 221:219–223, 2000.
- [71] O. Pietzch, A. Kubetzka, M. Bode, and R. Wiesendanger. *Science*, 292:2053–2056, 2001.
- [72] S. A. Chambers and S. A. Joyce. *Surface Science*, 420:111–122, 1999.

- [73] S. A. Chambers, S. Thevuthasan, and S. A. Joyce. *Surface Science*, 450:273–279, 2000.
- [74] A. V. Mijiritskii, M. H. Langelaar, and D. O. Boerma. *Journal of Magnetism and Magnetic Materials*, 21:278–282, 2000.
- [75] R. Wiesendanger, I. V. Shvets, D. Bürgler, G. Tarrach, H.-J. Günderodt, and J.M.D. Coey. *Zeitschrift für Physik B: Condensed Matter*, (86):1–2, 1992.
- [76] G. Tarrach, D. Burgler, T. Schaub, R. Wiesendanger, and H. J. Guntherodt. *Surface Science*, 285:1–14, 1993.
- [77] R. Jansen, V. A. M. Brabers, and H. Vankampen. *Surface Science*, 328:237–247, 1995.
- [78] R. Souda, Y. Hwang, T. Aizawa, W. Hayami, K. Oyoshi, and S. Hishita. *Surface Science*, 387:136–141, 1997.
- [79] L. P. Zhang, M. Li, and U. Diebold. *Surface Science*, 412–413:242–251, 1998.
- [80] G. P. Lopinski, D. D. M. Wayner, and R. A. Wolkow. *Nature*, 406:48–51, 2000.
- [81] Bartosz A. Grzybowski, Howard A. Stone, and George M. Whitesides. *Nature*, 405:1033–1036, 2000.
- [82] V. V. Bel'kov, J. Hirschinger, V. Novák, F.-J. Niedernostheide, S. D. Ganichev, and W. Prettl. *Nature*, 1999.

- [83] V. V. Bel'kov, J. Hirschinger, D. Schowalter, F.-J. Niedernostheide, S. D. Ganichev, W. Prettl, D. Mac Mathúna, and V. Novák. *Physical Review B*, 61(20):13698–13702, 2000.
- [84] Sh. K. Shaikhutdinov, W. Weiss, and R. Schlögl. *Applied Surface Science*, 161:497–507, 2000.
- [85] B. Stanka, W. Hebenstreit, U. Diebold, and S. A. Chambers. *Surface Science*, 448:49–63, 2000.
- [86] Scott A. Chambers. *Surface Science Reports*, 39:105–180, 2000.
- [87] Sh. Shaikhutdinov, M. Ritter, and W. Weiss. *Physical Review B*, 62(11):7535–7541, 2000.